Title
Highly Sensitive SERS Immunosensor via Extrinsic Nano-Stress Sensing

Author
Apontti, Leonard James

Publication Date
2018

UNIVERSITY OF CALIFORNIA
RIVERSIDE

Highly Sensitive SERS Immunosensor via Extrinsic Nano-Stress Sensing

A Thesis submitted in partial satisfaction
of the requirements for the degree of

Master of Science

in

Chemical and Environmental Engineering

by

Leonard James Apontti

September 2018

Thesis Committee:
    Dr. Ruoxue Yan, Chairperson
    Dr. Xin Ge
    Dr. Bryan Wong

The Thesis of Leonard James Apontti is approved:

Committee Chairperson

University of California, Riverside

Acknowledgments

I would like to thank my advisor, Dr. Ruoxue Yan for granting me the opportunity to not only work in her lab but for allowing me to really utilize my degrees on a research topic that I am really excited to see where it eventually leads. She was an excellent advisor who was always open to talk and provide guidance and support throughout my research which I am deeply thankful for.

Within the Yan Lab, I would also like to thank all of my lab mates: Dr. Sanggon Kim, Yangzhi Zhu, and Ning Yu for the many late lab nights spent together, discussing research, working on experiments, and just learning more about each other. I would also like to extend my thanks to those in Dr. Ming Liu's lab whom we often work with: Xuezhi Ma, Qiushi Li, and Da Xu. I will miss the time spent together with everyone and I also wish the best of luck for them and their research.

I would like to give a special thank you to my good friend Miles Bergeson, for always being there when I needed him, believing in me, and for always reminding me when I needed to take a break. Thank you for all the fun study sessions, helping me work through the logic and theory of chemistry related problems, and for always patiently listening to me when I needed to practice any presentations.

Most importantly, I would like to thank my family and loved ones for always believing in me and supporting me when I needed it. Without their constant love, support, and personal sacrifices, I would not be in such a position to succeed. Never before did they doubt my abilities to succeed academically despite not showing it early on. It was through them that I awakened a love for learning and I am deeply grateful for it. Thank you all!

ABSTRACT OF THE THESIS

Highly Sensitive SERS Immunosensor via Extrinsic Nano-Stress Sensing

by

Leonard James Apontti

Master of Science, Graduate Program in Chemical and Environmental Engineering
University of California, Riverside, September 2018
Dr. Ruoxue Yan, Chairperson

Biosensors have begun to attract and find widespread use in the medical field due to their potential for ultrasensitive detection, and as a reliable, high-throughput, and nondestructive diagnostic immunoassay, specifically aimed towards the early screening of cancer. Specifically, there is need to screen the early stages of tumor growth, as 90% of all cancer related deaths are due to metastasis. Matrix metalloproteinase-14 (MMP-14) is an important target for cancer research due to its ability to induce tissue remodeling, extracellular matrix degradation, tumor invasion and angiogenesis. Surface Enhanced Raman Spectroscopy (SERS) has emerged as a popular method of detection due to the high optical enhancement offered by the surface plasmon resonances (SPRs) of metallic nanostructures while preserving the structural specificity, rapid screening, and high flexibility of Raman spectroscopy. The direct SERS analysis of biomolecules often suffer from poor selectivity and sensitivity due to their weak Raman activities, lack of characteristic functional groups/polarizable moieties, and poor surface selection rules with the nanoparticle surface. This study hopes to take advantage of a novel indirect approach termed “nano-stress” sensing which provides an excellent alternative to conventional direct sensing. In short, a Raman reporter with a highly resolved, well characterized spectrum is chemically functionalized with a biorecognition element (e.g. antibodies) and undergoes a change in peak intensity or position in response to a molecular recognition event (e.g. antibody-antigen binding). Chapter 2 describes the synthesis of silver octahedral nanoparticles using a modified polyol process and their assembly into a large-scale, close-packed, two-dimensional, thin film SERS platform, using a homemade Langmuir-Blodgett (LB) trough. SEM images reveal many well-ordered, close-packed polycrystalline domains scattered throughout. Chapter 3 presents the fabrication of the SERS immunosensor using a self-assembled monolayer (SAM) of 4-MBA, its chemical modification to bind to Fab3A2, and the detection of cdMMP-14 through extrinsic nano-stress sensing. Optimization experiments using TRIS Buffer indicate that a 0.1M/0.1M EDC/NHS solution at pH 6.0 with stirring gives the highest 4-MBA conjugation (~50%). About 38.58% Fab3A2 conjugation was observed along with the successful sensing of the biorecognition event between Fab3A2 and cdMMP-14 at various concentrations. A maximum frequency shift of $0.95\pm0.37\text{cm}^{-1}$ was observed for $5\text{x}10^{-7}$M cdMMP-14. A linear semilog relationship (R^2=97.79%) was also observed giving the equation $y = 0.31136x + 2.9109$ for the concentration range $5\text{x}10^{-7}$M to $5\text{x}10^{-10}$M. Control experiments shows slight to relatively no binding with cdMMP-9 as well as minimal non-specific protein adsorption therefore confirming the specificity of the immunosensor.

Table of Contents

Acknowledgments .... **iv**
ABSTRACT OF THE THESIS .... **v**
List of Figure .... **viii**
Chapter 1: Introduction **1**
  1.1 Background and Motivation 1
  1.2 Methods of Detection 2
  1.3 SERS – Background and Principles 4
  1.4 SERS Based Substrates 12
  1.5 Objective of Work 14
  1.6 References 16
Chapter 2: Langmuir-Blodgett Thin Film Assembly of Octahedral Silver Nanoparticles **20**
  2.1 Introduction 20
  2.2 Experimental Methods 22
  2.3 Results and Discussion 25
  2.4 Conclusions 30
  2.5 References 31
Chapter 3: Highly Sensitive SERS Immunosensor for the Detection of cdMMP-14 Based on Extrinsic Nano-Stress Sensing **33**
  3.1 Introduction 33
  3.2 Experimental Methods 37
  3.3 Results and Discussion 38
  3.4 Conclusions 49
  3.5 References 50
Chapter 4: Conclusions and Future Work **54**
4.1 References: **57**

List of Figure

Figure 1-1: a.): “Quality Factor”, Q, of localized surface plasmon resonances with respect to wavelength for selected metallic NPs in an air medium. The shaded region corresponds to Q values where EFs of at least 10^5 can be obtained. b.): The real (a) and imaginary (b) parts of $\epsilon(\omega)$ for Au and Ag....7

Figure 1-2: Electric field enhancement contours for a triangular shaped Ag nanoparticle with a vertical (left) and a horizontal (right) electric field polarization at 700nm. The red arrows point to the areas with the highest EM enhancement....9

Figure 1-3: Coupled electric field enhancement factors for a nanoparticle dimer with a 2nm nanogap at 559nm and polarized along the vertical axis....10

Figure 2-1: SEM images of the as-prepared silver nanocrystal solution using the modified polyol process as the reaction proceeds with time, from (a) cubes, to (b) truncated cubes, to (c) truncated octahedra, and to (d) octahedra shaped nanoparticles....26

Figure 2-2: UV-Visible absorption spectra of cubes, truncated cubes, truncated octahedra, and octahedra shaped silver nanoparticles with inserts of each respectively....27

Figure 2-3: Schematic of the constructed Langmuir-Blodgett trough where (a) is a top-down view, (b) and (c) are a side, and lengthwise cross section respectively, and (d) is the Delrin push bar. The insert shows the completed trough and push bar used for all thin film experiments....28

Figure 2-4: Typical close packed silver octahedral nanoparticle thin film produced with the home-made Langmuir-Blodgett trough at (a) 20µm, (b) 10µm, (c) 5µM, and (d) 0.5µM magnification....29

Figure 3-1: Characteristic normalized SERS 4-MBA spectra produced on the octahedral thin film substrate in (a) air and (b) in pH solutions, 3.0, 7.4, and 10....39

Figure 3-2: Reaction scheme for capturing TRIS on the 4-MBA functionalized silver nano-octahedral (AgNO) thin film surface....40

Figure 3-3: (a)-(b) SERS spectra of TRIS conjugated to 4-MBA after EDC/NHS activation with varying EDC and NHS concentrations in air. Peak intensity of 1589cm^{-1} over 1370cm^{-1} is plotted against molar ratios of [NHS]/[EDC] to the right of each respective group of spectra. The dashed line indicates the most optimal condition....41

Figure 3-4: SERS spectra taken in HEPES buffer of TRIS conjugated to 4-MBA after varying EDC/NHS activation pH from (a) 5.9 to 7.5 and from (b) 5.9 to 5.0 with the percentage of COO- Peak reduction labeled next to each spectrum. (c) Percent of COO- Peak reduction at 1370cm^{-1} is plotted against pH...43

Figure 3-5: SERS spectra taken in HEPES buffer of TRIS conjugated to 4-MBA with increasing EDC/NHS activation time from 1- 4 hours. The bottom condition tested 1 hour with stirring. Percentage of COO- peak reduction is labeled next to each respective spectrum...44

Figure 3-6: SERS spectra of Fab3A2 conjugated to 4-MBA and Fab3A2:cdMMP-14 with percentage of COO- peak reduction labeled next to each respective spectrum..................45

Figure 3-7: (a) SERS spectra of the 4-MBA/Fab3A2 bound substrate after exposure to cdMMP-14 of various concentrations. (b) Semilog plot of the absolute peak shift as a function of cdMMP-14 concentration with respect to the peak located at 1080cm^{-1}...........46

Figure 3-8: SERS spectra of the 4-MBA/Fab3A2 bound substrate after exposure to cdMMP-14...47

Figure 3-9: (a) SERS spectra of 4-MBA with no EDC/NHS activation after adding Fab3A2 and cdMMP-14. (b) Zoom-in of the spectral region at 1080cm^{-1} with frequency shifts listed after each step...48

Chapter 1: Introduction

1.1 Background and Motivation

Over the past decade through the application of nanoscale materials, there has been a surge of sensor-based devices that are smaller and more compact then previous. Biological based sensors, or "biosensors", have been attracting a lot of attention in the fields of materials science and nanotechnology, due to their potential for high specificity, sensitivity, portability, and low cost. In short, a biosensor is a molecular device which can detect and transform a biochemical molecular-recognition event, into an electrical, thermal, optical, or other measurable analytical signal.[1] It consists of two main components: the sensor element which is capable of recognizing the presence of a specific analyte, using biorecognition elements like receptors, enzyme, antibody, etc.; and the signal transduction element that converts the binding event information into a measurable output signal.[1-2] The use of nano-based materials as the electronic and optical signal transducer element, has paved the way for the novel design of biosensing devices and research. This has led to significant device miniaturization, and the enabling of lower detection limits, down to even single biomolecule detection[3], and zeptomolar concentrations.[4]

This ultrasensitive biosensing has found widespread use in the medical field as a reliable, rapid, high-throughput, and nondestructive diagnostic immunoassay technique for disease-related biomarkers, most notably for tumor and cancer detection. Current methods of cancer screening however, are either highly invasive, require significantly high concentrations, or are only observable when visible changes to a tissue have already occurred.[5-6] In too many cases, the cancer has already metastasized and the probability of patient survival is low, even with medical intervention. The early detection and diagnosis of cancer is therefore critical and desirable for the successful treatment of the disease. In doing so, it reduces the risk of metastasis and increases patient survival rates by improving the efficiency of existing treatments when administered early on. Highly sensitive, quantitative diagnostics are therefore critical and vital for measuring ultralow cancer marker levels present during the early stages of the disease.

1.2 Methods of Detection

Fluorescence based methods have been extensively used with biosensor devices to analyze a variety of biomolecular interactions such as antigen-antibody[7-8], protein-protein[9-10], and enzyme-substrate[11-12], among others. Although highly sensitive, they require lengthy labeling steps, which increases not only the sample preparation time, but complicates the experimental process as well. In addition, in order to obtain quality images with the same level of sensitivity and specificity that traditional pathology imaging techniques enjoy, potentially invasive fluorescent labels must be used, which can interfere significantly with biological processes.[13]. In recent years, detection with label-free techniques have attracted considerable attention in biosensor development with Raman based spectroscopy techniques, such as surface plasmon resonance (SPR), localized surface plasmon resonance (LSPR), and surface enhanced Raman spectroscopy (SERS), being the most attractive. In addition, based on the molecule and the intrinsic nature of the Raman effect, spectra can be collected over a wide spectral region spanning from the UV to near-infrared. This flexibility provides a greater degree of experimental control that is lacking in other analytical techniques, especially fluorescence spectroscopy where the choice of excitation frequency is limited by the chosen fluorescent analyte.[14]

Raman spectroscopy has been explored for biomedical applications as an effective analytical technique due to its high spatial resolution, multiplexing capability, low background signal and distinct chemical spectra.[15] It provides a detailed optical molecular "fingerprint" of the biochemical composition of cells and tissues, without the need of external labels and is obtained via scattered light. This Raman scattering process occurs in response to the inelastic scattering of photons as a result of the interaction between incoming light and the electron cloud of a molecule.[14] Most of the scattered photons conserve the same energy as the incident photons (Reighley Scattering), while a small fraction of them either gain (anti-Stokes Scattering) or lose (Stokes Scattering) energy due to energy transfer between scattering partners. This energy difference corresponds directly to the characteristic energies of the vibrational states of the molecule which are in turn based on the structural characteristics of the molecules chemical bonds. Since these energy levels are unique for every molecule, Raman spectra are therefore highly specific and provide detailed chemical and structural information.[16] This can be used to study changes in the molecular composition of affected tissues by providing a clear signature for the presence of disease-related biomarkers in a sample. This valuable information can be used by physicians for real time diagnosis and has already been used to characterize cancers in various organs such as the esophagus[17-18], breast[19-20], lung[21-22], bladder[23-24], and skin[25-26].

Despite these capabilities however, the Raman effect produces an extremely weak signal due to low Raman cross-sections and since roughly 1 in 10^7 photons have the desired energy difference[16, 27] This inherent weakness in sensitivity is a key limitation of Raman spectroscopy. Longer exposure times and higher laser powers are often required to compensate in order to detect lower concentrations of molecules, which can severely damage biological samples.[14-15, 27-28] Fortunately, this limitation can be bypassed by enhancing the weak intensity of the Raman signal using the localized surface plasmon resonance (LSPR) generated in the near-field of metallic nanostructures. Molecules on or near the surface exhibit significantly enhanced Raman signals, with potential detection limits down to the single molecule level ($10^{11\text{-}12}$ enhancement), therefore terming this application Surface-Enhanced Raman Spectroscopy (SERS).[15] This technique combines the structural specificity, rapid screening, and high flexibility of Raman spectroscopy, with the optical signal amplification provided by metal nanostructures.[14]

1.3 SERS – Background and Principles

The SERS signal enhancement is directly related back to the basic principles of Raman scattering. The magnitude of scattered light is directly related to the polarizability of the molecule which interacts with the local incident electromagnetic (EM) field as shown[29]:

$$\mu_{\mathrm{ind}} = \alpha_{\mathrm{molecule}} E_{\mathrm{loc}}(\omega_{\mathrm{inc}}) \tag{1.1}$$

where μ_{ind}, is the induced dipole moment, $\alpha_{\mathrm{molecule}}$, is polarizability tensor of the molecule of interest, E_{loc}, is the local electric field intensity at the molecule, and ω_{inc}, is the frequency of the incident light. Equation 1.1 therefore describes the two main multiplicative mechanisms behind SERS to increase the overall Raman signal: EM and chemical enhancement (CE), where the electric field and molecule polarizability are increased respectively.

EM enhancement is often the dominating mechanism and can be described by the electromagnetic model. It depends on the Surface Plasmon Resonance (SPR) of metallic nanoparticles, i.e. the collective oscillation of free electrons at the metal surface due to interactions with external propagating EM waves. These electronic oscillations can be resonantly excited, allowing for enhanced electric fields near the metal nanoparticle surface where the total magnitude of the enhancement is given by the Local Field Intensity Enhancement Factor (LFIEF).[30-31]

$$\mathrm{LFIEF}(r,\omega) = \left|\frac{E_{\mathrm{loc}}(r,\omega)}{E_{\mathrm{inc}}(r,\omega)}\right|^2 \tag{1.2}$$

Equation 1.2 describes this increase in the intensity of the EM field at a specific point, *r*, on the nanoparticle surface, and frequency, ω, where E_{loc} and E_{inc} are the amplitudes of the local and incident electric field respectively. For a single molecule located on or near the surface of the nanoparticle, the SERS EM enhancement factor (EF), SM-$\mathrm{EF}_{\mathrm{EM}}$, depends on both the incoming light, ω_{inc}, and outgoing Raman-scattered light, ω_{s}, frequencies[30-32]:

$$\mathrm{SM}-\mathrm{EF}_{EM} = \mathrm{LFIEF}(\omega_{\mathrm{inc}}) \times \mathrm{LFIEF}(\omega_{\mathrm{s}}) \approx \mathrm{LFIEF}(\omega_{\mathrm{inc}})^2 = \left|\frac{E_{\mathrm{loc}}(r)}{E_{\mathrm{inc}}(r)}\right|^4 \tag{1.3}$$

Equation 1.3 therefore describes the EM mechanism as a two-fold EF. As the incident light approaches the metal surface, it couples with the plasmonic oscillations of the nanostructure resulting in a sharply enhanced amplitude of the EM field, subjecting the molecule of interest to a much stronger E_{loc}. [30, 33] The second enhancement occurs due to the coupling between the outgoing Raman scattered photons and the nanoparticle plasmon. Since ω_{vib} is generally small (not always true), $\omega_{\mathrm{s}} = \omega_{\mathrm{inc}} - \omega_{\mathrm{vib}} \approx \omega_{\mathrm{inc}}$, can be simplified, leading to an approximated $|E|^4$ field EF.[30, 33] Although this formula makes many simplifications, such as ignoring polarization issues between incoming and scattered fields, it provides a useful estimate for actual experimental SERS enhancements.

The CE mechanism reflects the increase of the Raman polarizability tensor and consequently the Raman cross-section. There are three possible routes in which this enhancement can occur: (1) Ground state CE, where molecules are not bound to the nanoparticle surface, or (2) Resonance Raman enhancement, and (3) Charge-Transfer (CT) enhancement, where the molecules are covalently bound to the metal surface.[27] The ground state CE occurs due to the presence of the metal perturbing the molecules electronic structure, which induces a slight shift or chance in its electronic distribution, or cross-section. [27] For resonance Raman and CT enhancement, the direct binding creates a metal-molecule complex which changes the intrinsic polarizability of the molecule.[27] For resonance Raman, this new complex creates a new electronic state where the frequency of the incoming light coincides with a resonant electronic transition. For CT enhancement, charge transfer can occur between the molecule and nanoparticle metal surface if the Fermi level of the metal is in between the HOMO and LUMO energies of the molecule. The metal acts like a charge-transfer intermediate where incoming light resonantly excites an electron from the metals Fermi level to the LUMO of the molecule, which subsequently relaxes back to the metal. During these electronic excitations for both resonance Raman and CT enhancement, vibrational modes can undergo changes in its bond length or force constant

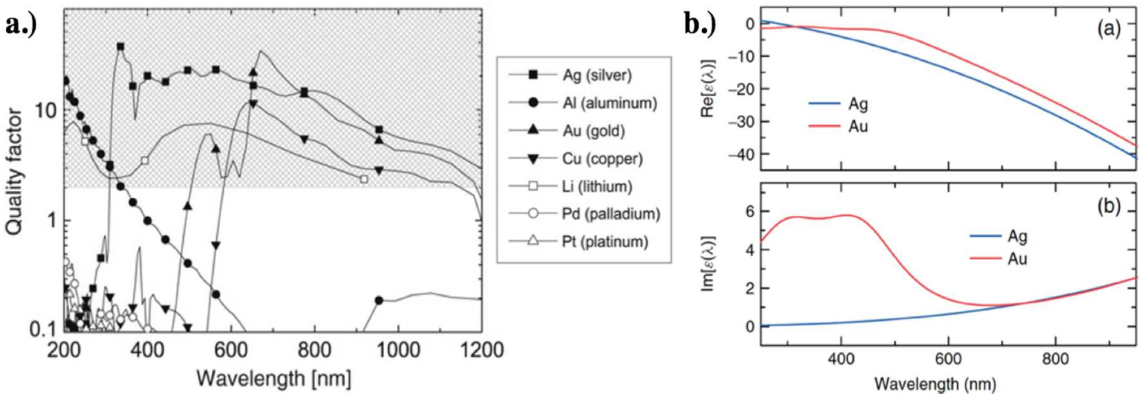

Figure 1-1: a.): "Quality Factor", Q, of localized surface plasmon resonances with respect to wavelength for selected metallic NPs in an air medium. The shaded region corresponds to Q values where EFs of at least 10^5 can be obtained.[31] b.): The real (a) and imaginary (b) parts of $\epsilon(\omega)$ for Au and Ag. [30]

thereby increasing the polarizability and Raman cross-section of the molecule. The CE mechanism contributes an overall 10-10^2 enhancement and occurs together with the EM mechanism. Both mechanisms therefore offer an approximated 10^6-10^8 SERS enhancement for single molecules located at the hottest spots, allowing for single molecule resolution, with potential to reach up to 10^{12} with further optimization of the chosen nanoparticle.[14, 27]

As discussed prior, the EM mechanism is strongly based on the collective oscillation of conducting electrons on the metallic nanoparticle surface. These SPR's are heavily dependent on the optical properties of the nanoparticle and are based on several factors such as its composition, geometry, size, and surrounding medium. [34] These optical properties can be described by a frequency dependent, complex dielectric constant, $\epsilon(\omega)$[27]:

$$\epsilon(\omega) = \epsilon_r(\omega) + i\epsilon_i(\omega) \tag{1.4}$$

where sub *r* is the real component and relates to the resonance conditions of the metal, and sub *i* denotes the imaginary component which is related to its absorption.[30-31] Figure 1.1a illustrates the quality factor, Q, for selected metallic NP in an air medium across various wavelengths and can be defined as[31]:

$$Q = \frac{\omega(d\epsilon_r/d\omega)}{2(\epsilon_i(\omega))^2} \tag{1.5}$$

The Q value is a dimensionless unit of measure that describes the resonant conditions of the electrons on the metal nanoparticle surface. Materials with large Q values experience less electronic dampening and therefore resonate at greater amplitudes, generating larger EM EFs. It is therefore clear from equation 1.5 that Q values are large when ϵ_i is small. From the image, Ag, Au, and Cu are the best materials to use for a surface-enhancing substrate when excited from the near-UV to the near-IR region. In fact, Au and Ag NP's are the most widespread source of SERS substrates, with Cu being rarely used due to its high oxidative nature.[30-31] Figure 1.1b shows the real (a) and imaginary (b) parts of $\epsilon(\omega)$ for Au and Ag. Using these complex dielectric functions along with Mie theory and a discrete dipole approximation, we can calculate all the electromagnetic properties of a material with different geometries.[30]

$$p \propto \frac{\epsilon(\omega) - \epsilon_M}{\epsilon(\omega) + \epsilon_M} \tag{1.6}$$

$$p \propto \frac{\epsilon(\omega) - \epsilon_M}{\epsilon(\omega) + 2\epsilon_M} \tag{1.7}$$

Equations 1.6 and 1.7 illustrate these geometry-induced resonances and describes the magnitude of the induced dipole, p, for a metallic 2D cylinder and a 3D sphere respectively,

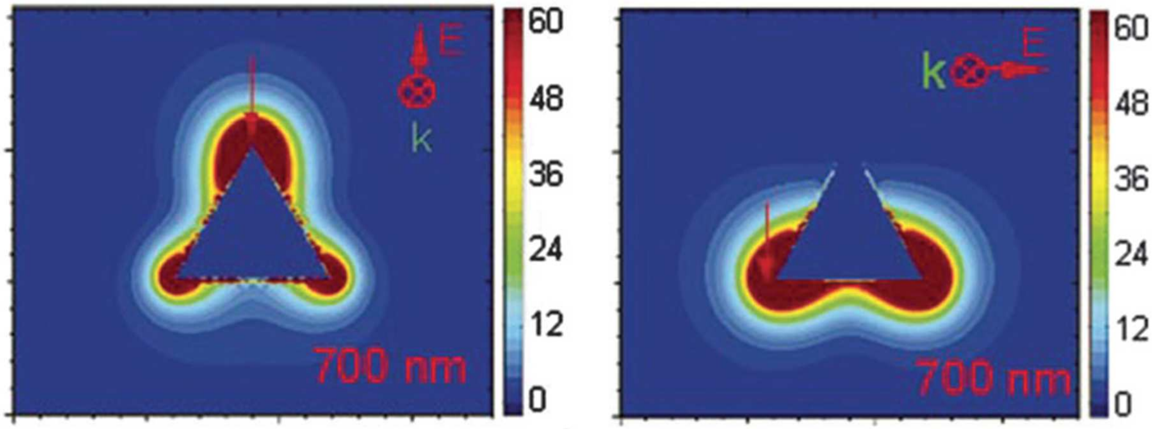

Figure 1-2: Electric field enhancement contours for a triangular shaped Ag nanoparticle with a vertical (left) and a horizontal (right) electric field polarization at 700nm. The red arrows point to the areas with the highest EM enhancement.[35]

where ϵ_M is the dielectric constant for the surrounding medium. These induced dipoles have a small dependence on ϵ_M, and become red shifted in a media as ϵ_M increases. Since ϵ_i is best small, large SERS enhancement can be obtained at the wavelengths of the incident or scattered radiation, when $\epsilon_r(\omega)$ approaches $-\epsilon_M$ for a cylinder and $-2\epsilon_M$ for a sphere. With these equations and Figure 1.1a, it is clear that Ag outperforms Au due to Au's higher absorption (large $\epsilon_i(\omega)$) over the UV to visible range ($\lambda \leq 700$nm) while only being comparable to Ag in the near- and far-IR regions. In the case for a molecule on a nanoparticle sphere with radius, *r*, these local field enhancements decrease rapidly with increasing distance, *d*, from the metallic surface with a decay of $EM_{sphere} \propto (r/(r+d))^{12}$. [32] This geometry-based dependence allows for plasmonic tunability and engineering for high EFs. As the geometry of the nanoparticle becomes more complex, the magnitude of the EF varies depending on its orientation with respect to the incident electric field as illustrated in Figure 1.2, with most of the enhancement being localized at the corners. Nanomaterials

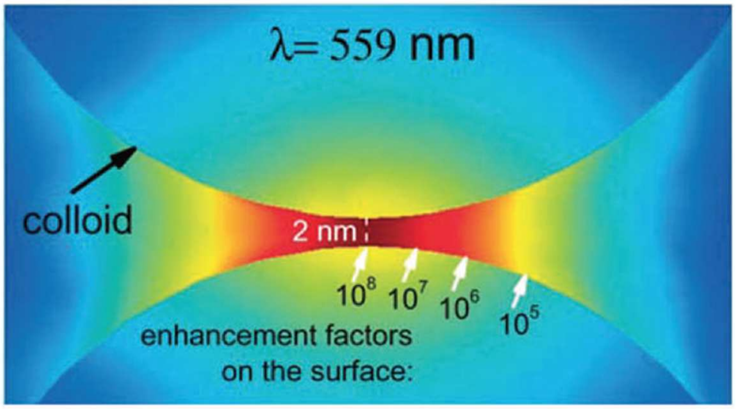

Figure 1-3: Coupled electric field enhancement factors for a nanoparticle dimer with a 2nm nanogap at 559nm and polarized along the vertical axis.[35]

with sharp corners or edges, offer higher signal enhancement then spherical or oval shaped nanoparticles at resonance due to the "lightning rod" effect, where the EM energy is confined at these pointed edges leading to strongly enhanced electric fields.[30-32, 35] Size is also an important factor, where LSP resonances red shift as nanoparticle size increases and dampens due to increasing radiation loss and the appearance of multipolar resonances that do not couple to light as effectively.[30-32, 35]

So far, only single nanoparticle EF's and how they can be affected have been discussed, but rarely is only one nanoparticle, or one molecule of interest used in experiments. Intense plasmonic hot spots can be induced in response to interacting nanoparticles in close mutual proximity. This enhancement is due to the plasmonic coupling between two or more nanoparticle dipoles as they come closer together, therefore red shifting the LFIEF. In the simplest case, the interaction energy between two nearby dipoles can be modeled as such[36]:

$$V \propto \frac{p_1 p_2}{r^3} \tag{1.8}$$

where p_1 and p_2 are the magnitudes of the dipole movement of nanoparticle 1 and 2, and r is the interparticle distance. As shown in equation 1.8 and Figure 1.3, this interaction energy is sufficiently strong as in the case of nearly adjacent nanoparticle spheres and decreases drastically as the distance between the two increases. The electric field is highly concentrated in the middle between the two nanoparticles with EFs reaching up to 10^8 (10^{10}-10^{12} if utilizing the lightning rod effect)[32, 37], and weakens with increasing distance from the center. As a result, it follows a characteristic long-tail distribution where the probability of a molecule finding a hot spot with the highest enhancement is low relative to the total surface area between the two dimers. [30, 32]. In experiments, we often work with many molecules of interest that are spread across the surface of our SERS substrate. As a result, each molecule experiences a very different EF depending on plasmonic hot spot locations. It is therefore more useful to obtain an average-EF of the SERS substrate[14, 32]:

$$\text{Average EF} = \frac{I_{SERS}/N_{Surf}}{I_{RS}/N_{Vol}} \tag{1.9}$$

where I_{SERS} and I_{RS} are the SERS and Raman intensities respectively; and N_{Surf} and N_{Vol} are the average number of molecules per scattering volume, and the average number of molecules adsorbed onto the metal surface per same scattering volume, respectively.[14] Average EF values typically range between 10^4-10^6, due to the combination of few highly enhancing hot spots, and many weakly enhancing sites on the metallic surface.[32, 37] Using these concepts and principles discussed thus far, largely enhancing SERES platforms for SERS based spectroscopy, can be engineered to develop highly sensitive substrates.

1.4 SERS Based Substrates

The successful fabrication, stability, and reproducibility of SERS based substrates are an important step for practical SERS applications. Prior limitations due to the irreproducibility of nanomaterial synthesis and substrate fabrication have hampered progression for wide scale use.[14, 27, 30, 32] Recent advances in nanoscience and nanofabrication within the past decade have allowed for the development of reliable, stable, reproducible, and rationally designed SERS substrates that have found widespread use across many fields of science using either a top-down or bottom-up approach.[2, 14] The top-down approach typically utilizes lithography or ion-beam, based techniques, to fabricate complex nanostructures directly on the substrate surface. Although these techniques offer great control over the fabrication process, along with great reproducibility and sensitivity, they require complex procedures, are highly expensive, and time-consuming to produce. The bottom-up approach uses chemically synthesized nanoparticles, typically though wet chemistry methods or deposition-based techniques, and are either used in suspension or are assembled onto a solid substrate. This method allows for simple manipulation to create nanoparticles of various sizes, shapes, as well as compositions, and offers great sensitivity, in addition to being quick, simple, and cost-effective to synthesize. Although it offers many advantages, both spot-to-spot and batch-to-batch reproducibility, along with synthesis control are often limiting factors for this approach.[2, 14] Recent progress in wet chemical nanosynthesis techniques however, has helped curb these disadvantages, allowing for greater experimental control and reproducibility in producing nanoparticles of various shapes and homogenous sizes. Stabilizers for example, such as poly(vinyl alcohol), poly(vinylpyrrolidone), or sodium dodecyl sulfate can be used to prevent aggregation and allow for greater control over the resulting size and shape of the nanoparticle, allowing for improved batch-to-batch reproducibility.[38] As a result, these wet chemical synthesis methods offer promising potential to produce reliable, stable, sensitive, and reproducible SERS based substrates that are cost-effective and quick to produce. The choice of SERS based substrate however, depends entirely on the intended application and what type of sensing the experiment calls for.

For biosensor applications, SERS detection of biological molecules can be accomplished with two methods: intrinsic and extrinsic sensing. Intrinsic SERS detection requires the molecule of interest to be close to or on the metal surface, either through physisorption or chemisorption in order to produce a characteristic spectral signature of the biomolecule. This method is more reliable then extrinsic sensing but suffers from poor selectivity and sensitivity due to the analytes large size relative to the SERS hotspots, poor surface selection rules with the nanoparticle, and its generally weak Raman activities.[14, 37, 39] Extrinsic SERS detection on the other hand is an indirect method of detection that uses the SERS signal of a Raman reporter molecule attached to the metal surface, and not the target analyte. These probe molecules provide a sharp, clear, intense, and characteristic SERS fingerprint spectrum that is sensitive to changes in its local environment due to molecular events, leading to changes in either the spectrum or intensity of the SERS profile. As a result, this technique offers higher sensitivity over intrinsic sensing, but is limited by its reproducibility due to the nonspecific binding of the target biomolecule. This can easily be solved by chemically modifying the reporter molecules surface groups, to allow for the functionalization of a specific biorecognition element such as an antibody onto the nanoparticle surface. Changes in spectra are therefore often stress-induced and occur in response to the reorientation of the label molecule with respect to the plasmonic surface and/or the deformation of its molecular structure.[40-41] This novel “nano-stress” SERS immunoassay platform is highly sensitive to the presence of a specific target antigen and can be used for in vitro and in vivo SERS diagnostics. In addition, a major advantage is that a wide range of labels are available that are easily distinguishable using only a single excitation source. This can allow for the simultaneous detection of multiple biomolecules without the need for additional separation procedures.[32]

1.5 Objective of Work

Based on the aforementioned information, SERS and SERS based biosensor platforms have become a popular topic of interest towards the early detection of cancer in healthcare and medicine due to its intrinsically sensitive nature. In doing so, it can allow for the selective and rapid point-of-care testing needed for improved disease diagnosis, monitoring, and resulting patient prognoses. Despite the advances made in recent nanosynthesis and nanostructure design, most biosensor substrate fabrication procedures are either expensive, complicated, or time-consuming. As a result, there is a need for a biosensor that is not only quick, reliable, and sensitive, but cheap and easy to produce. In addition, we hope to exploit the use of this nano-stress mechanism to allow for highly sensitive detection. The objective of this dissertation is therefore divided into two main goals. 1.) The facile synthesis of octahedral silver nanoparticles and their assembly into a thin film SERS substrate using the Langmuir-Blodgett technique. 2.) Fabrication of a

Fab3A2-conjugated 4-mercaptobenzoic acid (4-MBA) self-assembled monolayer to detect cdMMP14 via extrinsic nano-stress sensing. Chapter 2 describes the assembly of the SERS substrate using octahedral shaped silver nanoparticles synthesized with wet chemical methods, and their organization into a close packed monolayer thin film using a simple homemade Langmuir-Blodgett trough. Chapter 3 presents the fabrication of the SERS immunoassay biosensor using a self-assembled monolayer of 4-MBA, its chemical modification to bind to Fab3A2, and the detection of cdMMP-14 through extrinsic nano-stress sensing. Chapter 4 gives the concluding summary of the work done and ideas for future studies.

1.6 References

[1] Ali, J., Najeeb, J., Ali, M. A., Aslam, M. F., and Raza, A. “Biosensors: Their Fundamentals, Designs, Types and Most Recent Impactful Applications: A Review”. *Journal of Biosensors & Bioelectronics*. 8. 2017. 1-9.

[2] Ju, H., Zhang, X., and Wang, J. “Chapter 18: Nanobiosensing for Clinical Diagnosis”. *NanoBioscience: Principles, Development and Application.* New York: Springer, 2011. 425-452. Ebook.

[3] Litterford, R.E., Graham, D., Smith, W.E., and Khan, I. “Surface-Enhanced Raman Scattering (SERS), Applications. *Encyclopedia of Spectroscopy and Spectrometry*. Cambridge, MA: Academic Press, 2011. 389-395. Ebook

[4] Choi, C. and Yau, S-T. “Ultrasensitive Biosensing on the Zepto-Molar Level”. *Biosensors and Bioelectronics*. 26. 2011. 3386-3390.

[5] Frangioni, J.V. “New Technologies for Human Cancer Imaging”. *Journal of Clinical Oncology*. 26. 2008. 4012-4021.

[6] Kalinich, M. and Haber, D.A. “Cancer Detection: Seeking Signals in Blood”. *Science*. 359. 2018. 866-867.

[7] Goldman, R. D. “Antibodies: Indispensable Tools for Biomedical Research”. *Trends in Biochemical Sciences*. 25. 2000. 593-595.

[8] Guo, H., Zhou, X., Zhang, Y., Gu, C., Song, B., Shi, H. “Kinetic Analysis of a High-Affinity Antibody/Antigen Interaction Performed by Planar Waveguide Fluorescence Immunosensor”. *RCS Advances*. 6. 2016. 13837-13845.

[9] Senutovitch, N., Vernetti, L., Boltz, R., DeBiasio, R., Gough, A., and Taylor, D.L. “Fluorescent Protein Biosensors Applied to Microphysiological Systems”. *Experimental Biology and Medicine*. 240. 2015. 795-808.

[10] Ibraheem, A., and Campbell, R.E. “Design and Applications of Fluorescent Protein-Based Biosensors”. *Current Opinion in Chemical Biology*. 14. 2010. 30-36.

[11] Klos-Witkowska, A. “Enzyme-Based Fluorescent Biosensors and Their Environmental, Clinical and Industrial Applications”. *Polish Journal of Environmental Studies*. 24. 2015. 19-25.

[12] Amine, A., Mohammadi, H., Bourais, I., and Palleschi, G. “Enzyme Inhibition-Based Biosensors for Food Safety and Environmental Monitoring”. *Biosensors and Bioelectronics*. 21. 2006. 1405-1423.

[13] Schaederle, M. D., Kalasinsky, V. F., Luke, J. L., Lewis, E. N., Levin, I. W., and Treado, P. J. “Raman Chemical Imaging: Histopathology of Inclusions in Human Breast Tissue.” *Analytical Chemistry*. 68. 1996. 1829-1833.

[14] Guerrini, L. and Graham, D. “Molecularly-Mediated Assemblies of Plasmonic Nanoparticles for Surfaced-Enhanced Raman Spectroscopy Applications”. *Chem. Soc. Rev.* 41. 2012. 7085-7107.

[15] Jeon, T. Y., Kim, D. J., Park, S-G., Kim, S-H., and Kim, D-H. “Nanostructured Plasmonic Substrates for Use as SERS Sensors”. *Nano Convergence*. 3. 2016. 1-20.

[16] Zhang, Y., Hong, H., and Cai, W. “Imaging with Raman Spectroscopy”. *Current Pharmaceutical Biotechnology*. 11. 2010. 654-661.

[17] Bohorfoush, A.G. “New Diagnostic Methods for Esophageal Carcinoma”. *Recent Results in Cancer Research*. 155. 2000. 55-62.

[18] Sharma, N., Takeshita, N., and Ho, K.Y. “Raman Spectroscopy for the Endoscopic Diagnosis of Esophageal, Gastric, and Colonic Diseases”. *Clinical Endoscopy*. 49. 2016. 404-407.

[19] Gao, P., Han, B., Du, Y., Zhao, G., Yu, Z., Xu, W., Zheng, C., and Fan, Z. “The Clinical Application of Raman Spectroscopy for Breast Cancer Detection”. *Journal of Spectroscopy*. 2017. 2017.

[20] Haka, A.S., Shafer-Peltier, K.E., Fitzmaurice, M., Crowe, J., Dasari, R.R., and Feld, M.S. “Diagnosing Breast Cancer by Using Raman Spectroscopy”. *Proceedings of the National Academy of Sciences of the United States of America*. 102. 2005. 12371-12376.

[21] McGregor, H.C., Short, M.A., McWilliams, A., Shaipanich, T., Ionescu, D.N., Zhao, J., Wang, W., Chen, G., Lam, S., and Zeng, H. “Real-Time Endoscopic Raman Spectroscopy for *in vivo* Early Lung Cancer Detection”. *Journal of Biophotonics*. 10. 98-110.

[22] Huang, Z., McWilliams, A., Lui, H., McLean, D.I., Lam, S., and Zeng, H. “Near-infrared Raman Spectroscopy for Optical Diagnosis of Lung Cancer”. *International Journal of Cancer*. 107. 2003. 1047–1052.

[23] Kerr, L.T., Lynn, T.M., Cullen, I.M., Daly, P.J., Shah, N., O’Dea, S., Malkin, A., and Hennelly, B.M. “Methodologies for Bladder Cancer Detection with Raman Based Urin Cytology.” *Analytical Methods*. 8. 4991-5000.

[24] de Jong, B.W.D., Schut, T.C.B., Maquelin, K., Kwast, T.V.D., Bangma, C.H., Kok, D-J., and Puppels, G.J. "Discrimination Between Nontumor Bladder Tissue and Tumor by Raman Spectroscopy". *Analytical Chemistry*. 78. 7761-7769.

[25] Zhao, J., Zeng, H., Kalia, S., and Lui, H. "Using Raman Spectroscopy to Detect and Diagnose Skin Cancer *In Vivo*". *Dermatologic Clinics*. 35. 2017. 495-504.

[26] Caspers, P.J., Lucassen, G.W., and Puppels, G.J. "Combined *In Vivo* Confocal Raman Spectroscopy and Confocal Microscopy of Human Skin". *Biophysical Journal*. 85. 2003. 572–580.

[27] Khetani, A., Momenpour, A., Tiwari, V. S., and Anis, H. "Surfaced Enhanced Raman Scattering (SERS) Using Nanoparticles". *Silver Nanoparticle Applications in the Fabrication and Design of Medical and Biosensing Devices*. New York: Springer, 2015. 47-70. Ebook.

[28] Prochazka, M. "Chapter 7: Medical Applications of SERS". *Surface-Enhanced Raman Spectroscopy: Bioanalytical, Biomolecular and Medical Applications*. New York: Springer, 2016. 149-211. Ebook.

[29] Prochazka, M. "Chapter 2: Basic of Raman Scattering (RS) Spectroscopy". *Surface-Enhanced Raman Spectroscopy: Bioanalytical, Biomolecular and Medical Applications*. New York: Springer, 2016. 7-20. Ebook.

[30] Etchegoin, P. G. and Le Ru, E. C. "Chapter 1: Basic Electromagnetic Theory in SERS". *Surface Enhanced Raman Spectroscopy: Analytical, Biophysical, and Life Science Applications*. Weinheim, Germany: Wiley-VCH, 2011. 1-38. Ebook.

[31] Le Ru, E. C. and Etchegoin, P. G. "Chapter 3: Introduction to Plasmons and Plasmonics". *Principles of Surface Enhanced Raman Spectroscopy and Related Plasmonic Effects.* Amsterdam, Elsevier, 2009. 121-183. Ebook.

[32] Prochazka, M. "Chapter 3: Basics of Surface-Enhanced Raman Scattering (SERS) Spectroscopy". *Surface-Enhanced Raman Spectroscopy: Bioanalytical, Biomolecular and Medical Applications*. New York: Springer, 2016. 21-60. Ebook.

[33] Yamamoto, Y. S., Ozaki, Y., and Itoh, T. "Recent Progress and Frontiers in the Electromagnetic Mechanism of Surface-Enhanced Raman Scattering." *Journal of Photochemistry and Photobiology C: Photochemistry Reviews*. 21. 2014. 81-104.

[34] Sannomiya, T. and Voros, J. "Single Plasmonic Nanoparticles for Biosensing". *Cell Press*. 29. 2011. 343-351.

[35] Hao, E. and Schatz, G. C. “Electromagnetic Fields Around Silver Nanoparticles and Dimers”. *Journal of Chemical Physics*. 120. 2004. 357-366.

[36] Halas, N. J., Lal, S., Chang, W. S., Link, S., and Nordlander, P. “Plasmons in Strongly Coupled Metallic Nanostructures.” *Chemical Reviews*. 111. 2011. 3913-3961.

[37] Radziuk, D. and Moehwald. H. “Prospects for Plasmonic Hot Spots in Single Molecule SERS Towards the Chemical Imaging of Live Cells.” *Phys. Chem. Chem. Phys.* 17. 2015. 21072-21093

[38] Khodashenas, B. and Ghorbani, H.R. “Synthesis of Silver Nanoparticles with Different Shapes”. *Arabian Journal of Chemistry*. 1. 2014. 1-16.

[39] Prochazka, M. “Chapter 5: Biomolecular SERS Applications ”. *Surface-Enhanced Raman Spectroscopy: Bioanalytical, Biomolecular and Medical Applications*. New York: Springer, 2016. 21-60. Ebook.

[40] Kho, K.W., Dinish, U.S., Kumar, A., and Olivo, M. “Frequency Shifts in SERS for Biosensing”. *ACS Nano*. 6. 2012. 4892-4902.

[41] Perumal, J., Kong, K.V., Dinish, U.S., Bakker, R.M., and Olivo, M. “Design and Fabrication of Random Silver Films as Substrate for SERS Based Nano-Stress Sensing of Proteins”. *RCS Advances*. 4. 2014. 12995-13000.

Chapter 2: Langmuir-Blodgett Thin Film Assembly of Octahedral Silver Nanoparticles

2.1 Introduction

The ability of nearly adjacent Ag nanocrystals to produce strongly enhancing hotspots, has led to a continual push to construct SERS platforms that take advantage of this highly enhancing effect. For practical SERS applications however, the ability to generate simple, large-scale nanocrystal assemblies, has often been a limiting factor for development.[1-2] Ideally, an attractive strategy should be quick, cost-effective, defect tolerant, and versatile, such that a variety of different materials can be used.[3] Among the various assembly techniques developed to organize metal nanoparticles into well-ordered arrays[2,4], the Langmuir-Blodgett (LB) assembly has become an increasingly promising candidate. It is a robust, interfacial self-assembly technique, originally developed to create molecular monolayers, that has been adapted to arrange nanomaterials of various geometries, compositions, and sizes, into highly ordered, large-scale, 2D domains.[5] In short, NPs are dispersed drop-wise over an air-water interface through the use of an organic non-polar solvent, and are allowed to reach an equilibrium surface pressure on the surface. Using a mobile barrier, the film is subject to a uniaxial, isothermal compression at controlled speeds. As the surface pressure of the monolayer increases, nanostructures on the aqueous subphase begin to assemble into densely packed, ordered arrays that can reach up to several square centimeters.[6] These colloidal films can then easily be transferred to a substrate though vertical dip coating, where a final, solid-state, cohesive thin film can be obtained. This technique therefore allows for the continuous manipulation of particle spacing and subsequent plasmonic tunability of resulting films. As discussed in Ch.1 however, changing the size and geometry of the nanoparticle used, in addition to their spacing, can allow for further EM enhancement of the SERS platform.

The need for a reliable synthesis technique to develop well-defined metal nanoparticles, and in large amounts, is therefore important. The polyol synthesis is a well-established, solution-based method, that produces Ag nanocrystals of uniform shapes and sizes.[7-10] For a typical synthesis, a polyol, such as ethylene glycol, propanediol, butanediol, glycerol, or pentanediol, acts as both a solvent and reductant.[11] An organic capping agent polyvinylpyrrolidone, PVP, and a Ag-salt precursor are added to a pre-heated polyol, resulting in the reduction of Ag^+ ions, and their subsequent nucleation and growth into Ag nanoparticles. As the reaction proceeds, PVP selectively adsorbs on the {100} facets of the Ag through its oxygen atoms, resulting in the preferential deposition on the poorly passivated {111} facets.[12-13] The resulting shape of the final NP depends on the type of seed that grows after nucleation, where single crystalline, singly twinned, and multiply twinned crystals result in nanocubes, right bipyramids, and pentagonal nanowires, respectively.[15-16] Nanocubes with well-defined facets and corners are preferred due to the lighting rod effect since they allow for EF's at least an order of magnitude higher then spherical shaped NP's.[13-14]. Through simple manipulating of the Ag-salt and PVP molar ratio, the synthesis can be directed towards a single crystalline morphology.[8, 12-13] In addition, the lattice strain induced by twinning results in high energy defects, making them highly reactive.[17-18] The presence of O_2 from the air and the introduction of trace Cl^- ions, allows for their selective oxidative etching, resulting in increased yields of single crystalline nanocubes.[9, 18-19] As the reaction proceeds, SERS enhancement increases as cubes transition to truncated cubes, then to cube-octahedra, and finally octahedra[19-20], with an EF reaching up to $10^{7\text{-}8}$ for well-ordered, close-packed, octahedral films.[21] These octahedral thin films therefore offer the potential to construct highly sensitive SERS substrates for early cancer detection.

Both the LB process and polyol synthesis offer quick, simple, and cost-effective ways to synthesize and assemble well-defined Ag polyhedral NPs into compact, large-area, highly enhancing SERS platforms. In this study, the facile synthesis of octahedral shaped silver nanoparticles using a modified polyol process, along with their nanoscale assembly into close-packed thin films, are reported. To further demonstrate the effectiveness of this technique, films were generated using a homemade Langmuir-Blodgett trough and were transferred to silicon wafer chips (~1μm^2) using a standard syringe pump. Characterization of the octahedral nanoparticles and the LB film are also provided.

2.2 Experimental Methods

Chemicals:

1,5 Pentanediol (PD) was purchased from Alpha Aesar. Silver Nitrate ($AgNO_3$), Ethanol Anhydrous (EtOH), and Chloroform ($CHCl_3$) were purchased from Thermo Fisher Scientific. Copper (II) Chloride Dihydrate ($CuCl_2$), and Polyvinylpyrrolidone (MW=55,000) (PVP), were purchased from Sigma-Aldrich. Ultrapure (R~18 MΩ) distilled water (dH_2O) was purified with a Barnstead E-Pure system from Thermo Fisher Scientific.

Instruments:

For all LB films, silicon wafer chips were cleaned using a Harrick Plasma PDC-32G Plasma Cleaner. An NE-1000 Programable Single Syringe Pump was used to transfer the films to the silicon substrate.

Synthesis of Octahedral AgNPs:

Octahedral AgNPs were prepared according to a previously reported polyol synthesis method with slight modification.[6] Briefly, an $AgNO_3$ precursor solution (120mM) was prepared in a glass vial by sonicating AgNO3 (0.20g) and 20µL of $CuCl_2$ (0.063M) in 1,5-pentanediol (10mL) until all crystals dissolved. Three additional $AgNO_3$ solutions (240mM) were also prepared in glass vials by sonicating $AgNO_3$ (0.40g) and 40µL of $CuCl_2$ (0.063M) in 1,5-pentanediol (10mL) until all crystals dissolved. In four separate vials, PVP (0.20g) was dissolved in 1,5-pentanediol (10mL). In a 100mL glass round bottom flask, 1,5 pentanediol (20mL) was heated for 10 min under continuous stirring using a temperature-controlled silicon oil bath set to 190^0C. The two precursor solutions were then added dropwise to the hot pentanediol at the following rates: 500µL of the 120mM $AgNO_3$ solution every minute and 250µL of the PVP solution every 30s. After complete addition of the 120mM $AgNO_3$ solution, the reaction is continued with the three 240mM $AgNO_3$ solutions at the same rates as above.

Purification of AgNPs:

The as-synthesized octahedral Ag colloidal solution was split evenly into six separate 50mL plastic centrifuge tubes and dispersed in ethanol for a total volume of 45mL. They were centrifuged at 9000 r.p.m for 20min. to isolate the silver nanocrystals from the pentanediol solvent. The supernatant was discarded, and the resulting precipitate was redispersed in 45mL ethanol through sonication. The wash process was repeated 5 times and collected at a final volume of 25mL. Afterwards the nanocrystal solution is carefully transferred into a 0.02 wt% solution of PVP in dH_2O (250mL) so that the final volume is 10 times the original volume of the nanocrystal solution. Using vacuum filtration, the solution was passed through a series of Durapore filters: 1.2, 0.8, 0.65, and 0.45 µm, supported on a glass frit. The purified octahedral solution was then centrifuged, redispersed, and stored in ethanol.

LB Trough Assembly:

A miniature LB trough was made using a 2.0"W x 3.5"L x 1.0"D polytetrafluoroethylene (PTFE) block at the University of California, Riverside, Machine Shop. The trough hole was centered and the dimensions are 1.0"W x 2.5"L x 0.5"D. In addition, 1/8"W x 2.5"L x ¼"D grooves were placed on either side of the trough hole to prevent spilling. A push bar was made using polyoxymethelene (POM), with dimensions: 0.5"W x 2.0"L x 0.5"D. A schematic of the final design is illustrated in Figure 2-3.

LB Assembly of Octahedra AgNPs:

The octahedral AgNP solution was allowed to settle completely overnight where one concentrated drop was taken from the bottom and suspended in a 3:22 $CHCl_3$:EtOH spreading solution. The LB trough and push bar were cleaned thoroughly with $CHCl_3$ and EtOH three times and dried under an N_2 stream to ensure a clean surface. The trough was filled with dH_2O (18 MΩ), and the water surface was cleaned by dragging the push bar across the water surface multiple times. Silicon wafer chips (~1µm^2) were cleaned by air plasma treatment on high setting for 10 minutes. The chips were submerged under the dH_2O surface and kept in place using reverse cross lock tweezers attached to a standard syringe pump. The spreading solution was then added dropwise to the dH_2O surface carefully and allowed to evaporate for 1 hr. to allow for the surface pressure to equilibrate. The film was compressed slowly to about half way where music was then played to create acoustic vibrations to help anneal the film (tracks with more bass give best results). Compression is complete when the film adopts a silver mirror-like appearance and slight wrinkles form on the edges of the push bar. The film was then transferred to the silicon substrate using the syringe pump at a rate of 0.3 mm/min.

Characterization:

UV-Vis excitation spectra were used to characterize the shape, size, and relative monodispersity of the colloidally prepared octahedral AgNPs, and were collected with a VWR UV-1600PC Spectrophotometer. Scanning Electron Microscopy (SEM) images were captured on an FEI Nova NanoSEM 450 to confirm the size and morphology of the NPs and to investigate the quality of the close packed thin films produced.

2.3 Results and Discussion

Characterization of Octahedral AgNPs:

The as-synthesized silver octahedra nanoparticles using a modified polyol process and their growth from nanocrystal polyhedra are shown in Figure 2-1 (a-d). For a metal with an *fcc* crystallographic structure such as Ag, the resulting surface energies are as follows: $\gamma_{\{111\}} < \gamma_{\{100\}} < \gamma_{\{110\}}$.[19] As mentioned prior, PVP selectively adsorb on the {100} facets of single crystalline seeds, resulting in the formation of nanocubes were Ag atoms

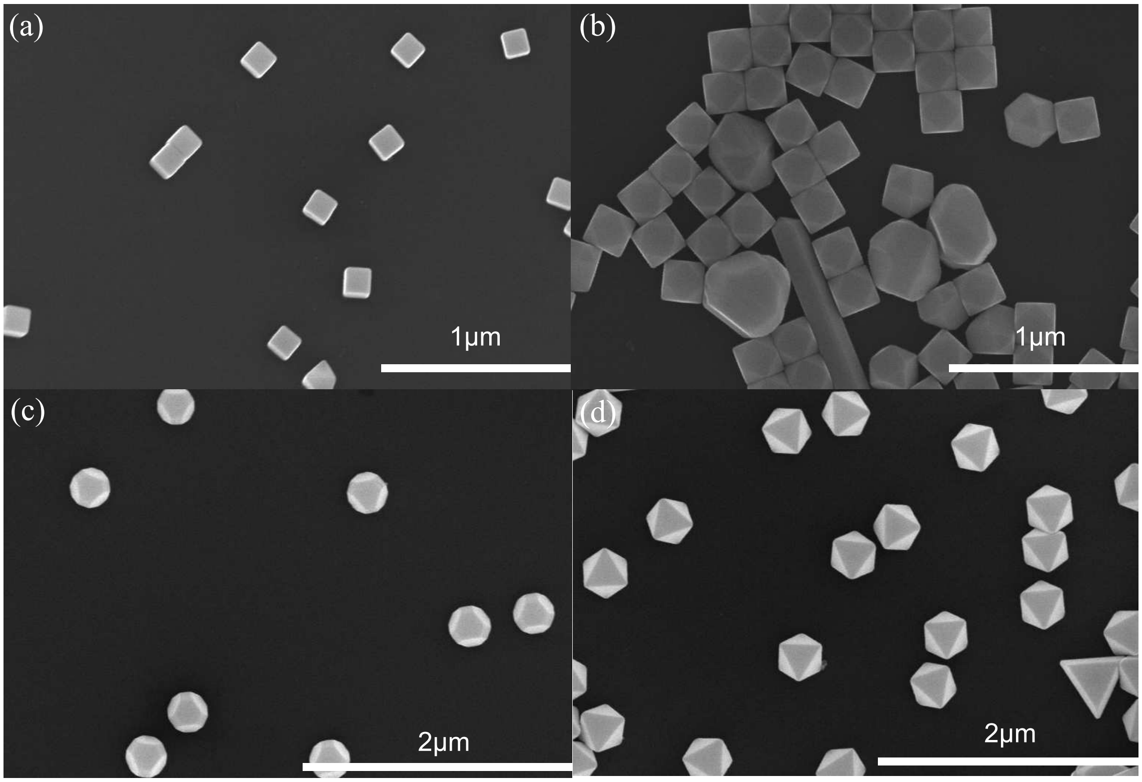

Figure 2-1: SEM images of the as-prepared silver nanocrystal solution using the modified polyol process as the reaction proceeds with time, from (a) cubes, to (b) truncated cubes, to (c) truncated octahedra, and to (d) octahedra shaped nanoparticles.

preferentially add to the {111} facets. As the reaction proceeds with time, a critical size is reached, and Ag atoms selectively deposit onto the {100} facets in an effort to lower the overall surface energy of the nanocrystal. This results in the growth of {100}-bound nanocubes to truncated cubes, truncated octahedra, and finally to {111}-bound octahedral nanocrystals. These clearly distinct geometric nanoparticles interact and couple with incoming light differently from each other and can therefore be easily characterized by UV-Vis as shown in Figure 2-2. The absorption spectra illustrate the differences in the local surface plasmon resonance (LSP) modes for each nanoparticle. For nanocubes with

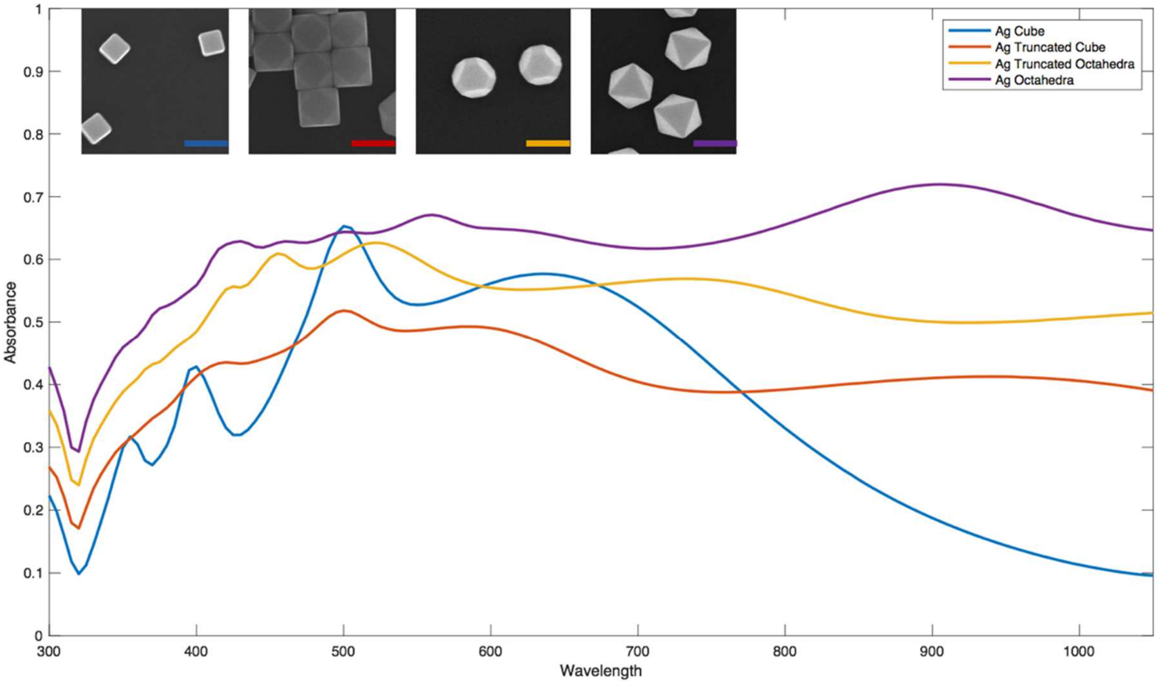

Figure 2-2: UV-Visible absorption spectra of cubes, truncated cubes, truncated octahedra, and octahedra shaped silver nanoparticles with inserts of each respectively.

edge lengths of ~145nm, there are six LSP resonances that have been previously reported[13], with four major modes located at the peaks 355, 400, 500, and 645nm. The first and second modes correspond to a dipolar (645nm), and a dominate quadrupolar (500nm) LSP mode respectively. As the particle size increases and transitions to truncated cubes with edge lengths of ~210nm, (and later to truncated octahedra with diameters of ~300nm), the quadrupolar mode disappears while the third and fourth LSP modes red shift to ~500nm and ~415nm, thereby dominating the spectra with increasing {111} facets. For octahedra shaped nanoparticles with edge lengths of ~310nm, the resulting optical signature is increasingly complex with several strong absorbance peaks ranging from 350nm to 1000nm. According to DDA calculations[13], these LSP modes are assigned to hexapolar and higher-order modes while the large broad peak at 915nm is primarily due to octupolar modes.

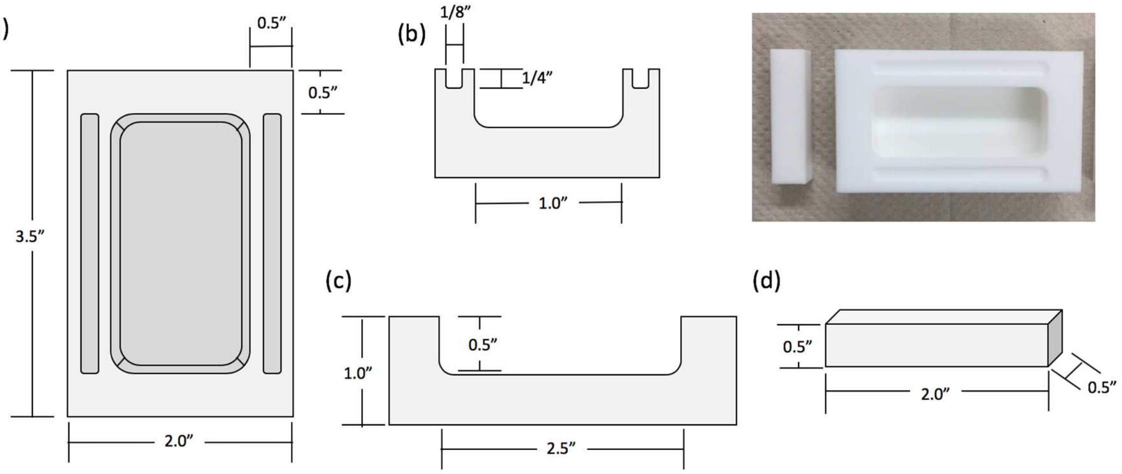

Figure 2-3: Schematic of the constructed Langmuir-Blodgett trough where (a) is a top-down view, (b) and (c) are a side, and lengthwise cross section respectively, and (d) is the Delrin push bar. The insert shows the completed trough and push bar used for all thin film experiments.

Characterization of Ag Octahedral Langmuir-Blodgett Films:

The fabricated Langmuir-Blodgett trough and push bar are illustrated schematically in Figure 2-3 (a-d) with an insert showing the completed trough used for all experiments. In tradition with conventional LB troughs, the main body was built using Teflon (PTFE) since it is chemically inert and therefore resistant to organic spreading solvents such as $CHCl_3$. The small dimensions for the body were chosen since the size of the silicon substrates used were small ($\sim 1 \mu m^2$) and therefore large thin films were not required. In doing so it also allows for small quantities of concentrated nanocrystals to be used to minimize waste. Delrin (POM) was used to construct the push bar due to its hydrophilic nature. Previous experiments with hydrophobic Teflon push bars, had difficulty maintaining film surface pressure due to nanocrystals sliding around the barrier. The Delrin push bar helped form a tight seal with the dH_2O surface, preventing the nanocrystals from sliding around the edges and allowed for consistent surface pressure during compression.

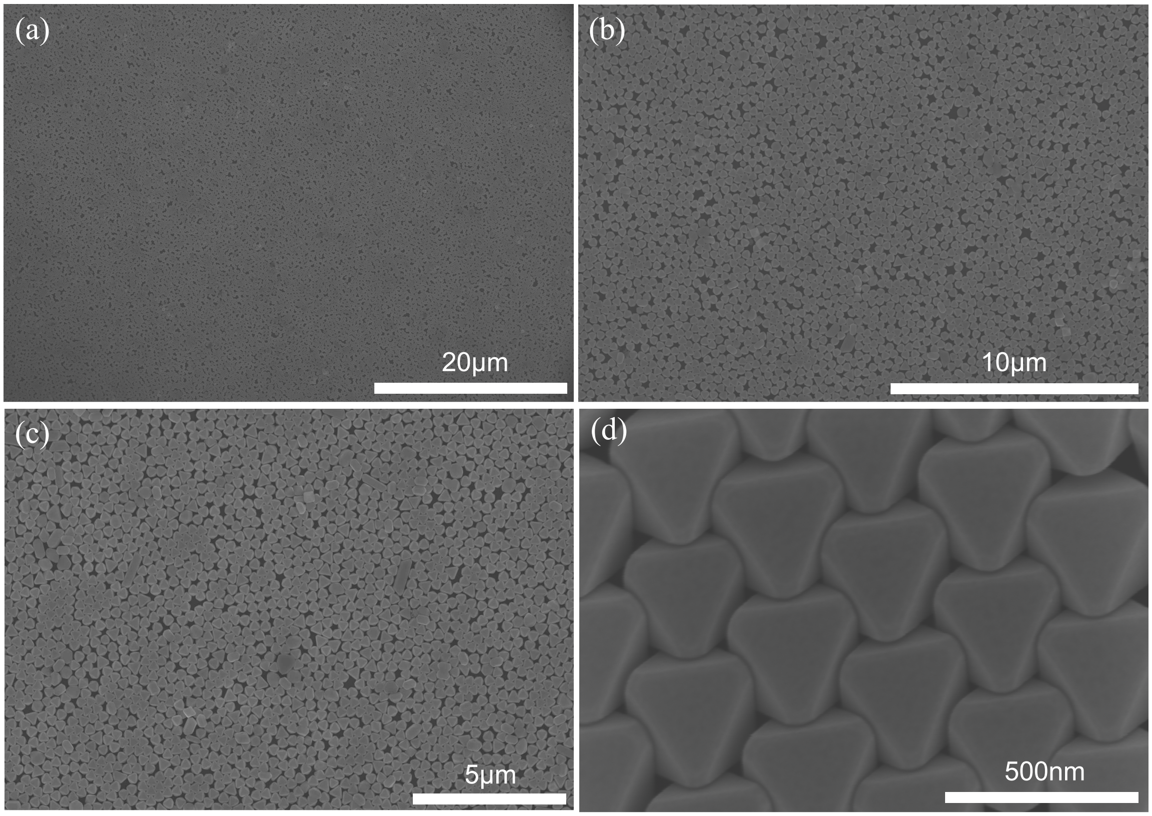

Figure 2-4: Typical close packed silver octahedral nanoparticle thin film produced with the home-made Langmuir-Blodgett trough at (a) 20μm, (b) 10μm, (c) 5μM, and (d) 0.5μM magnification.

Figure 2-4 (a-d) shows the SEM images used to characterize the resulting close packed Ag octahedral LB film typically produced with the homemade LB trough at increasing magnification. As shown in Figure 2-4 (a), large scale, two-dimensional film transfer was successfully obtained for most of the substrate. Unfortunately Figure 2-4 (b-c), show the presence of Ag nano-rods, -triangles, and -plates, that were not filtered out due to their relatively small sizes compared to the pore size of filters used, and may have hindered more large-scale, well-ordered arrays from forming. Looking closer at the SEM images however, reveals many well-ordered, close packed, polycrystalline domains of Ag octahedral nanocrystals scattered throughout the LB film. Figure 2-4 (d) reveal that these octahedra domains assemble into hexagonal lattices, where they lay flat on their triangular shaped faces to form interlocked triangles. These SEM images therefore suggest that the close-packed, two-dimensional silver octahedral nanocrystal LB films were successfully obtained.

2.4 Conclusions

For SERS immunosensor design, cost-effective and quick substrate fabrication are essential for biosensor applications. In this study, high-quality Ag octahedral nanocrystals were synthesized in large quantities using a modified polyol process and were assembled into large-scale, close-packed, two-dimensional LB thin films using a homemade LB trough. The Ag octahedral nanocrystals and their evolution from nanocubes, can easily be characterized using UV-Vis absorption spectra and SEM images. Calibration curves can also be constructed using each nanocrystals dominant LSP mode to easily control for size. A cheap and simple homemade LB trough and push bar were constructed while a standard syringe pump was used to transfer LB films from the dH_2O surface to the silicon substrate. Typical LB films produced with this experimental set-up, reveal large-area, close-packed, two-dimensional Ag octahedra nanocrystal assemblies necessary for sensitive SERS applications. The presence of nano-rods, -triangles, and -plates however, limit large-scale, well-ordered packing. Despite this, there were many well-ordered, polycrystalline domains scattered though out the substrate. This work helps illustrate the potential to construct simple, quick, and cost-effective SERS substrates without the need or use of cost-consuming laboratory equipment or procedures.

2.5 References

[1] Lee, Y.H., Lee, C.K., Tan, B., Tan, J.M.R., Phang, I.Y., and Ling, X.Y. “Using Langmuir-Schaefer Techniques to Fabricate Large-Area Dense SERS-Active Au Nanoprism Monolayer Films”. *Nanoscale*. 5. 2013. 6404-6413.

[2] Freeman, R.G., Grabar, K.C., Allison, G.K.J., Bright, R.M., Davis, J.A., Guthrie, A.P., Hommer, M.B., Jackson, M.A., Smith, P.C., Walter, D.G., and Natan, M.J. “Self-Assembled Metal Colloid Monolayers: An Approach to SERS Substrates”. *Science*. 1995. 267. 1629-1632.

[3] Tao, A., Huang, J., and Yang, P. “Langmuir-Blodgettry of Nanocrystal and Nanowires”. *Accounts of Chemical Research*. 41. 2008. 1662-1673.

[4] Velev, O. and Gupta, S. “Materials Fabricated by Micro- and Nanoparticle Assembly – The Challenging Path from Science to Engineering”. *Advanced Materials*. 2009. 21. 1897-1905.

[5] Kuo, T.R., Chen, Y.C., Wang, C.I., Shen, T.H., Wang, H.Y., Pan, X.Y., Liou, C.C., Chang, Y.H., Chen, Y.C., Wu, Y.W., Liu, Y.R., Lin, Y.H., Hu, C.C., and Chen, C.C. “Highly Oriented Langmuir-Blodgett Film of Silver Cubeoctahedra as an Effective Matrix-Free Sample Plate for Surface-Assisted Laser Desorption/Ionization Mass Spectrometry”. *Nanoscale*. 9. 2017. 11119-11126.

[6] Tao, A., Sinsermusksakul, P., and Yang, P. “Tunable Plasmonic Lattices of Silver Nanocrystals”. *Nature Nanotechnology*. 2. 2007. 435-441.

[7] Fievet, F. Lagier, J.P., Blin, B., Beaudoin, B., and Figlarz, M. “Homogeneous and Heterogeneous Nucleation in the Polyol Process for the Preparation of Micron and Submicron Size Metal Particles”. *Solid State Ionics*. 1989. 32. 198-205.

[8] Sun, Y. and Xia, Y. “Shape-Controlled Synthesis of Gold and Silver Nanoparticles”. *Science*. 2002. 298. 2176-2179.

[9] Wiley, B. Herricks, T., Sun ,Y., and Xia, Y. “Polyol Synthesis of Silver Nanoparticles: Use of Chlorine and Oxygen to Promote the Formation of Single-Crystal, Truncated Cubes and Tetrahedrons”. *Nano Letters*. 2004. 4. 1733-1739.

[10] Im, S.H., Lee, Y.T., Wiley, B., and Xia, Y. “Large-Scale Synthesis of Silver Nanocubes: The Role of HCl in Promoting Cube Perfection and Monodispersity”. *Angewandte Chemie*. 2005. 44. 2154-2157.

[11] Han, H.J., Yu, T., Kim, W.S., Im, S.H. “Highly Reproducible Polyol Synthesis for Silver Nanocubes”. *Journal of Crystal Growth*. 2017. 469. 48-53.

[12] Wiley, B., Sun, Y., Mayers, B., Xia, Y. “Shape-Controlled Synthesis of Metal Nanostructures: The Case of Silver”. *Chemistry A European Journal*. 2005. 11. 454-463.

[13] Tao, A., Sinsermsuksakul, P., and Yang, P. “Polyhedral Silver Nanocrystals with Distinct Scattering Signatures”. *Angewandte Chemie International Edition*. 2006. 45. 4597-4601.

[14] Rycenga, M., Kim, M.H., Camargo, P.H.C., Cobley, C., Li, Z.Y., and Xia, Y. “Surface-Enhanced Raman Scattering: Comparison of Three Different Molecules on Single-Crystal Nanocubes and Nanospheres of Silver”. *The Journal of Physical Chemistry A*. 2009. 113. 3932-3939.

[15] Rycenga, M., Cobley, C.M., Zeng, J., Li, W., Moran, C.H., Zhang, Q., Qin, D., and Xia, Y. “Controlling the Synthesis and Assembly of Silver Nanostructures for Plasmonic Applications”. *Chemical Reviews*. 2011. 111. 3669-3712.

[16] Polavarapu, L. Mourdikoudis, S. Pastoriza-Santos, I., and Perez-Juste, J. “Nanocrystal Engineering of Noble Metals and Metal Chalcogenides: Controlling the Morphology, Composition and Crystallinity”. *CrystEngComm*. 2015. 17. 3727-3762.

[17] Baletto, F. and Ferrando, R. “Crossover Among Structural Motifs in Transition and Noble-Metal Cluster”. *Journal of Chemical Physics*. 2002. 116. 3856-3863.

[18] Lofton, C., and Sigmund, W. “Mechanisms Controlling Crystal Habits of Gold and Silver Colloids”. *Advanced Functional Materials*. 15. 2005. 1197-1208.

[19] Xia, Y., Xiong, Y., Lim, B., Skrabalk, S.E. “Shape-Controlled Synthesis of Metal Nanocrystals: Simple Chemistry Meets Complex Physics?” *Angewandte Chemie International Edition*. 2009. 48. 60-103.

[20] Xia, Y., Gilroy, K.D., Peng, H.C., Xia, X. “Seed-Mediated Growth of Colloidal Metal Nanocrystals”. *Angewandte Chemie International Edition*. 2016. 55. 2-38.

[21] Mulvihill, M., Tao, A., Benjauthrit, K., Arnold, J., and Yang, P. “Surface-Enhanced Raman Spectroscopy for Trace Arsenic Detection in Contaminated Water”. *Angewandte Chemie International Edition*. 47. 2008. 6456-6460.

Chapter 3: Highly Sensitive SERS Immunosensor for the Detection of cdMMP-14 Based on Extrinsic Nano-Stress Sensing

3.1 Introduction

Despite its steady decline within the past decade in response to readily available and improved treatments, cancer remains a major public health concern and the second leading cause of death in the United States.[1] An estimated >1.6 million new cases and >0.6 million deaths were reported in 2017 alone, with metastasis acting as the leading cause of cancer-related deaths .[1-3] Limited progress has been made for the treatment of cancer metastasis with current treatments consisting mainly of chemotherapy and radiotherapy, and improved survival rates occurring due to early diagnosis and cancer growth inhibition.[3] As a result, there is an urgent need for the development of sensitive and specific methods that target the early stages of metastasis that is essential for the timely and successful treatment of the disease.

There are four major steps in cancer metastasis: detachment of the metastatic cells from the primary tumor, cell migration to different sites via the blood or lymphatic system, settlement in a new location, and growth at the distal site. These steps are inter-related and also heavily influenced by the tumor microenvironment, with the extracellular matrix emerging as a significant factor in influencing cancer progression.[4] Matrix metalloproteinases (MMPs) are a class of zinc-dependent endopeptidases that are responsible for tissue remodeling and extracellular matrix degradation, and have been extensively studied for metastasis prevention and inhibition.[4] They play vital roles in normal biological processes such as organismal growth and development, immune response mediation, and wound repair.[4] Many MMPs however, often correlate with pathological cancer progression[5], including cancer cell invasion[6], tumor angiogenesis and vasculogenesis[7], along with proliferation and apoptosis [8-9].Membrane type-1 MMP (MT1-MMP or MMP-14) for example is a membrane-tethered collagenase that is of particular interest due to its ability to promote cancer cell migration/invasion by reducing the physical barriers (collagen) that block tumor growth and metastatic spread. It acts as a pericellular collagenase by degrading fibrillar collagens (most abundant extracellular matrix component) types I-III, except type IV, which makes up the basement membrane.[10] Homodimerization of MMP-14 however, can activate MMP-2 into proMMP-2, which can degrade type IV collagen, causing effective tissue degradation, and thereby making a path for cancer migration.[10] In addition, it cleaves cell surface molecules laminin-5 $\gamma 2$, CD44, and pro-α_{v} integrin, which promotes cellular migration and invasion.[10-11] Elevated expression of MMP-14 has been found in various cancers, including breast[12], ovarian[13], nasopharyngeal[14], lung[15], colon[16], etc. and directly correlates with poor patient prognosis, blood vessel invasion, and high incidence of distant metastasis.[17]

Taking all this evidence into account, MMP-14 has become a promising target for therapeutic cancer treatment as well as an important regulatory enzyme for cancer research.[18] Many treatments however, failed early clinical trials due to the highly conserved catalytic mechanism and catalytic domain across the MMP family. As a result most peptide or small molecule inhibitors often promote broad spectrum inhibition across many MMPs, leading to undesired side effects such as inflammation and musculoskeletal pain.[19] Despite many MMPs acting as pro-tumorigenic, there are some that exhibit tumor-suppressing effects such as MMP-8[20], MMP-3[21], and MMP-12[22]. The specific and selective blocking/binding of individual MMPs is highly desirable not only for successful cancer treatment but for early cancer screening diagnostics as well. Recently, monoclonal antibodies with long, convex-shaped, camelid like paratopes were incorporated into human IgG allowing the antibody to target MMP-14 active pockets that are not accessible with conventional antibodies.[23] Specifically, Fab3A2 was reported by Nam et al. (2016) to bind to MMP-14 in the vicinity of the active pocket with a high 4.8nM affinity and a 9.7nM inhibiting potency towards protease cleavage activity.[23] These inhibitors therefore provide an excellent opportunity to be used towards the early detection/screening of elevated MMP-14 levels in patients.

Conventional methods for detecting MMPs include ELISA (enzyme-linked immunosorbent assays), zymography, near-IR optical imaging, fluorescence, SPR spectroscopy, and LC-MS/MS (liquid chromatography-mass spectroscopy).[24] As of late, ELISA remains the most widely adopted diagnostic technique for the quantitative detection of MMPs due to its convenient readout and high quantification accuracy, and has many commercially available kits. These assays however, can lead to imprecise and potentially misleading results due to lack of specificity (active vs. latent forms) or between specific MMPs and their TIMP complexes.[24] Sandwich ELISAs on the other hand, offer greater sensitivity and specificity, but require two different antibodies per MMP, and a separate assay plate must be used for the measurement of each MMP, thereby greatly increasing the cost and time of the assay.[24] In addition, these fluorescence-based immunoassays (e.g. ELISA) are limited in their choice of excitation frequency due to the chosen fluorescent analyte, and suffer from inherently wide fluorescent peaks (100-300nm).

SERS has long been considered as an effective choice for biological analysis due to its ability to retain the rich and structural information provided by Raman spectroscopy while overcoming its inherently weak signal intensity through the LSPR optical signal enhancement offered by well-defined metal nanostructures. SERS based immunoassays therefore have the potential for increased sensitivity over ELISA due to their highly resolved spectra with enhancement factors reaching as high as 10^{12} allowing for single molecule resolution and enhanced early detection.[25] The direct SERS measurement of small biomolecules (e.g. proteins and DNAs) however, remains challenging due to their relatively large (3-10nm) size compared to the SERS hotspots of well-packed nanostructures (sub-1nm gaps), making it highly unlikely for them to access these areas which provide the strongest signal enhancement. In addition, biomolecules lack highly polarizable moieties resulting in inherently weak Raman activities and often possess many similar functional groups which make it difficult for specific biomolecular characterization.

SERS “nano-stress” sensing is a novel indirect Raman sensing approach that provides an excellent alternative to conventional direct sensing.[26-27] In short, Raman labels with intense and characteristic SERS spectra are chemically functionalized with specific biorecognition elements (e.g. antibodies) and undergo changes in peak intensity or position in response to molecular recognition with the desired antigen. This analyte recognition event is often revealed by frequency shifts in the reporter molecules vibrational modes and occurs in response to the reorientation of the label molecule with respect to the plasmonic surface and/or deformation of its molecular structure.[28-29] As a result, this “nano-stress” sensing can allow for highly sensitive and specific quantitative biosensing as the degree of frequency shift is in direct correlation with the concentration of the target biomolecule and has been shown to provide up to sub-pM detection.[28-30]

3.2 Experimental Methods

Chemicals:

4-Mercaptobenzoic Acid (4-MBA), *N*-(3-Dimethylaminopropyl)-*N*′-Ethylcarbodiimide Hydrochloride (EDC), and Ethanol Anhydrous (EtOH), were purchased from Sigma Aldrich. *N*-Hydroxysuccinimide (NHS) was purchased from TCI Tokyo. All experiments used MES Buffer (50mM, pH 6.0) and HEPES Buffer (50mM, pH 7.5, NaCl, 150mM) solution. Fab3A2, cdMMP-14, and cdMMP-9 were obtained and purified from Dr. Xin Ge's Lab at the University of California, Riverside.

4-MBA Self-Assembled Monolayer:

Self-Assembled Monolayers (SAM's) of 4-MBA were formed by immersing the LB octahedral thin film substrate into a 3.0mM 4-MBA solution using nitrogen purged ethanol with stirring for 4hrs at room temperature. The substrate was then washed thoroughly with ethanol to remove any excess 4-MBA and dried under a stream of nitrogen.

Fab3A2 Binding:

After self-assembled monolayer formation of 4-MBA, the LB octahedral thin film substrate was submerged in a 0.1M/0.1M EDC/NHS solution using MES buffer (50mM, pH 6.0), for 3hr with stirring. The substrate was then taken out of the EDC/NHS activating solution and washed thoroughly in HEPES buffer before soaking in a 10μg/mL Fab3A2 solution suspended in HEPES buffer overnight at 4°C. The substrates were then thoroughly rinsed 4 times in HEPES buffer to remove excess Fab3A2.

CdMMP-14 Sensing:

The Fab3A2-bound substrate was immersed in HEPES solutions containing cdMMP-14 for 1hr at 4°C. The substrate was then thoroughly rinsed again 4 times in HEPES buffer to remove excess cdMMP-14. For negative control experiments, the Fab3A2-bound substrate was immersed in HEPES solutions containing cdMMP-9 for 1hr at 4°C, before thoroughly rinsing 4 times in HEPES buffer to remove excess cdMMP-9.

Characterization:

All Raman spectra were acquired using a Horiba LabRAM NT Raman microscope. The excitation source was a 532nm laser with a laser power of 0.6mW, 100μm diameter focal spot laser excitation, 10s integration time, and 2 accumulations. High-resolution Raman mapping images were obtained using a 50X objective lens, 600 and 1800 g/nm grating, and a 26.7μm mapping step over a 4900μm^2 mapping region. Each Raman spectra shown are an accumulation of 16 spectra. All samples were kept immersed in HEPES buffer during SERS measurements unless otherwise stated.

3.3 Results and Discussion

Characterization of 4-MBA SAM:

The SERS spectrum of the 4-MBA SAM produced on the LB octahedral thin film substrate is shown on Figure 3-1(a). As shown, the spectrum possesses many sharp, clearly

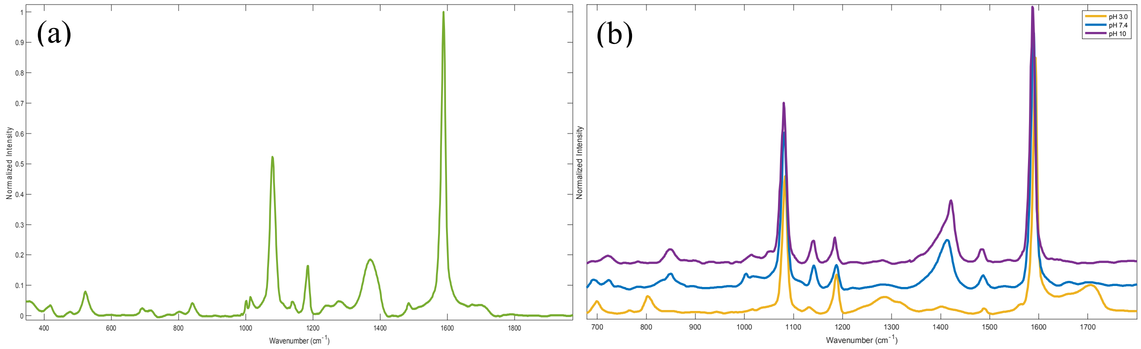

Figure 3-1: Characteristic normalized SERS 4-MBA spectra produced on the octahedral thin film substrate in (a) air and (b) in pH solutions, 3.0, 7.4, and 10.

distinct peaks, with the most prominent peaks located at 1589cm^{-1} (ν_{8a}, a$_1$) and 1080cm^{-1} (ν_{12}, a$_1$) belonging to the ring-breathing modes of the benzene ring, with 1080cm^{-1} being coupled with the ν(C-S) bending from the thiol group. In addition, the large broad peak at 1370cm^{-1} corresponds with ν_s(COO-) stretching mode, therefore indicating that a large number of surface carboxyl groups are in a deprotonated state. Several less intense vibrational modes are also present and have been assigned as such: 417cm^{-1} (ν_s(C-S) in-plane bending), 691cm^{-1}((C-H) out of plane deformation), 718cm^{-1}(γ(CCC) out-of-plane vibration), 840cm^{-1}(δ(COO-) in-plane deformation), 1000cm^{-1}and 1013cm^{-1}(v(CC) in-plane), 1140cm^{-1} (ν_{15}, b$_2$) and 1183cm^{-1}(ν_9, a$_1$) ((C-H) deformation bending), and 1710cm^{-1} (C=O stretching). Due to 4-MBA's large characteristic COO- stretching mode at 1370cm^{-1}, it is highly sensitive to changes in pH and can be used to help further characterize the resulting SAM. Figure 3-1(b) reveals how the 4-MBA spectrum changes with varying pH solutions, 3.0, 7.4, and 10. At pH 3, the ν_s(COO-) peak almost completely disappears, with a large increase at 1710cm^{1} (C=O stretching). This results in response to protonation of the carboxyl group with the 4-MBA molecule adopting a more perpendicular orientation with the Ag surface. As pH is increased, an intense red-shifted ν_s(COO-) peak emerges at

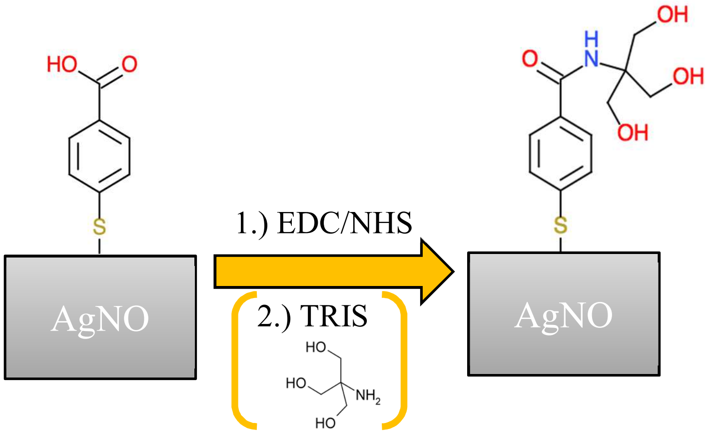

Figure 3-2: Reaction scheme for capturing TRIS on the 4-MBA functionalized silver nano-octahedral (AgNO) thin film surface.

1410cm^{-1} with increasing intensity from pH 7.4 to pH 10, while the C=O stretching mode disappears. Similar to before, this results due to deprotonation of the carboxyl group with the 4-MBA molecule adopting a more parallel orientation with Ag surface. Both results from Figure 3-1(a) and (b) match well with previously reported data.[31-32]

SERS Capture Substrate Optimization:

The reaction scheme for the immobilization of TRIS on the 4-MBA SAM is illustrated on Figure 3-2. TRIS buffer was used as a substitute for Fab3A2 in early experiments in order to optimize the device and as a means to minimize wasted Fab3A2. The first step of the reaction involves the activation of the carboxyl group with EDC. It is often used in protein synthesis and conjugation reactions due to its ability to couple carboxyl groups to primary amines and is a water soluble, zero-length crosslinking carbodiimide agent. For this study, EDC/NHS was used over traditional EDC due to the stability and longer half-life of the EDC/NHS intermediate thereby making it less easily hydrolyzed. In addition, the reaction would require everything to be mixed together, as such there is a high risk of EDC activating carboxyl groups on proteins causing them to conglomerate together.

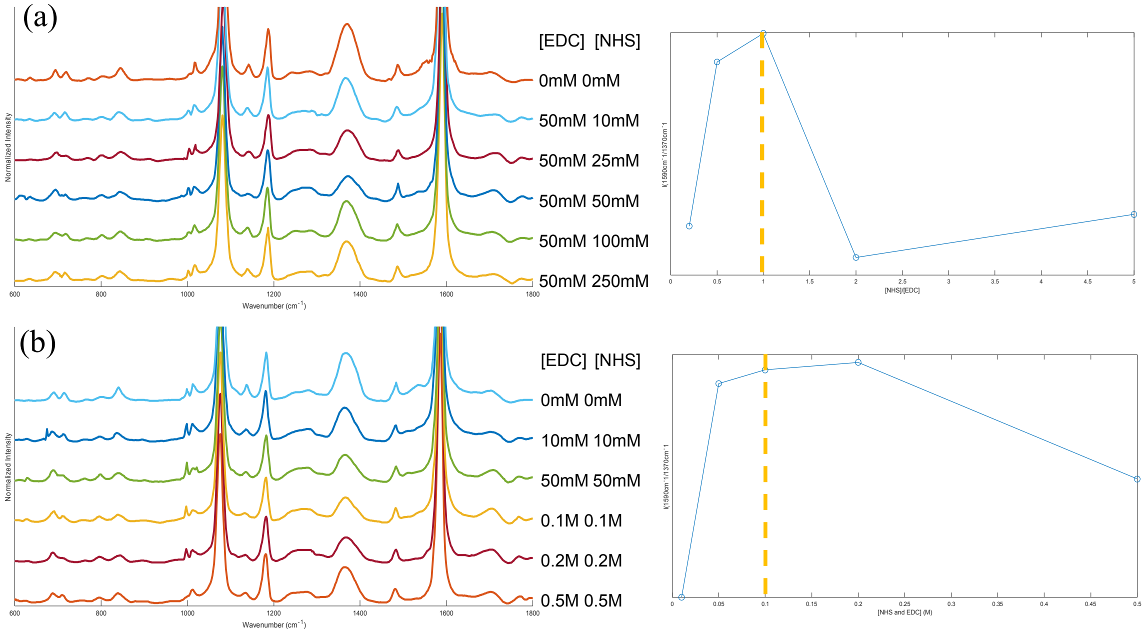

Figure 3-3: (a)-(b) SERS spectra of TRIS conjugated to 4-MBA after EDC/NHS activation with varying EDC and NHS concentrations in air. Peak intensity of 1589cm^{-1} over 1370cm^{-1} is plotted against molar ratios of [NHS]/[EDC] to the right of each respective group of spectra. The dashed line indicates the most optimal condition.

Despite the widespread use of the EDC/NHS chemistry, there has been no well-established protocol towards efficient activation. Many studies have varied important parameters such as EDC/NHS ratio, concentration, pH of activating solution, and activation time greatly [33-36], with the highest reported activation reaching 70% on PAA brushes.[33] As such, thoroughly investigating these important parameters are crucial to fully optimize the SERS capture substrate. Figure 3-3 (a) shows the SERS spectra of TRIS conjugated to the 4-MBA SAM after EDC/NHS activation at five varying ratios ([NHS]/[EDC]): 0.2, 0.5, 1.0, 2.0, and 5.0. Since effective binding replaces the -OH group with an -NH group on the 4-MBA surface, it is expected that the peaks associated with COO- such as 1370cm^{-1}(ν_s(COO-)) and 840cm^{-1}(δ(COO-) in-plane deformation) would disappear as previous reports have observed.[28-30, 30-33] The peak at 1370cm^{-1} was chosen since it is the most intense and sensitive to peak reduction. As the ratios approach 1:1, there is a significant decrease in the COO- peak height, which begins to increase again as [NHS] is increased. Plotting the ratio of the peak height at 1589cm^{-1} over 1370cm^{-1} with respect to the molar ratios of [NHS]/[EDC], it is clear that a molar ratio of 1:1 provided the most peak reduction for COO-. Similarly, Figure 3-3 (b) shows the SERS spectra of TRIS conjugated to the 4-MBA SAM after EDC/NHS activation at five varying concentrations: 0.01M, 0.05M, 0.1M, 0.2M, and 0.5M. As the concentration increases to 0.2M, maximum COO- peak reduction is reached according to the plot on the right of the spectra, which then subsequently decreases at 0.5M. Despite offering a larger COO- peak reduction, a concentration of 0.1M was chosen for two major reasons. First, the amount of peak reduction over 1.0M was relatively small (~1.0%) to justify a significant increase in EDC use. Second, large EDC/NHS concentrations run the risk of forming unreactive *N*-acylurea in which EDC undergoes an irreversible arrangement via an intermolecular acyl transfer or potential anhydride formation. [30-33] Fortunately anhydrides can still undergo the necessary reaction but regenerates one carboxyl group for every bound primary amine leading to poor binding efficiency. With that in mind, a 0.1M/0.1M EDC/NHS ratio was chosen for all experiments.

Figure 3-4 investigated the effect of EDC/NHS activation solution pH with respect to COO- peak reduction at 1370cm^{-1} under more (a) basic and (b) acidic conditions. Figure 3-4 (c) plots the cumulative results into one graph. As pH increases from 5.90 to 7.5, a steady increase in COO- peak intensity is observed, with a similar increase occurring as pH decreases from 5.90 to 5.0, although at a much slower rate. The steep decrease in

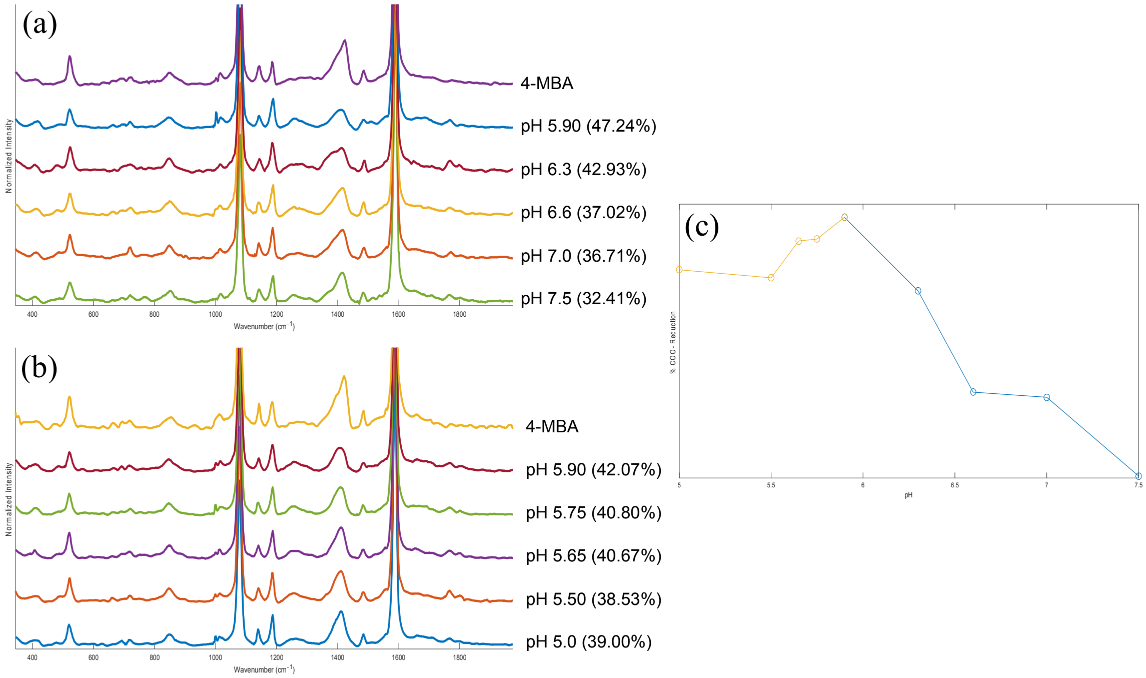

Figure 3-4: SERS spectra taken in HEPES buffer of TRIS conjugated to 4-MBA after varying EDC/NHS activation pH from (a) 5.9 to 7.5 and from (b) 5.9 to 5.0 with the percentage of COO- Peak reduction labeled next to each spectrum. (c) Percent of COO- Peak reduction at 1370cm^{-1} is plotted against pH.

%COO- reduction with basic pH may be attributed to hydrolysis of the NHS intermediate as increasing pH significantly decreases its half-life. Similarly, the slightly less decrease in %COO- reduction under acidic pH may be the result of potential anhydride formation, leading to a 1:1 regeneration of an undesired carboxyl group. From Figure 3-4 (c) it is clear that pH 5.90 (~pH 6.0) gives the best results.

The effects of EDC/NHS activation time on COO- peak reduction were explored in Figure 3-5 with percent of COO- peak reduction listed on the side of each spectrum. As activation time increases from 1-4 hrs. there is a steady decrease in the COO- peak. When stirring was employed for 1 hour however, a 6.5% increase in peak reduction was observed

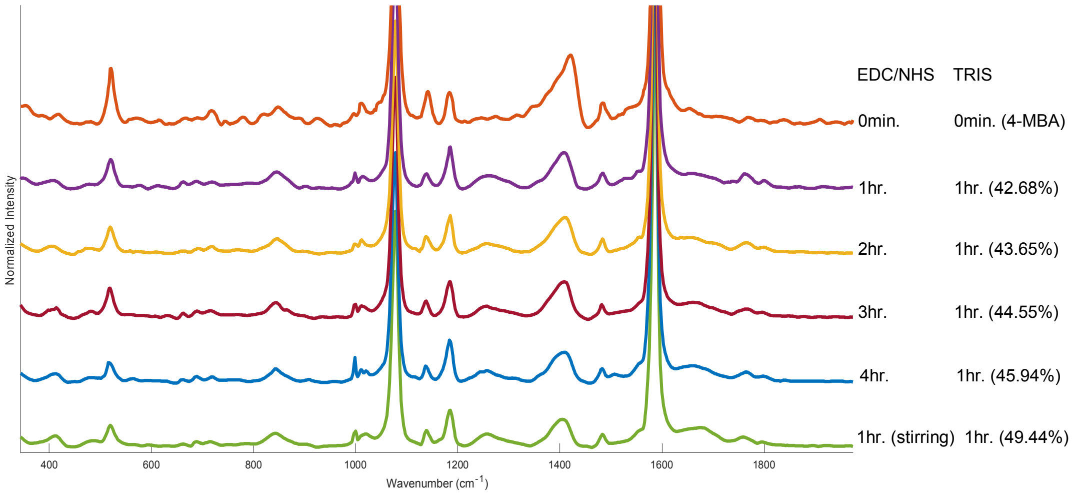

Figure 3-5: SERS spectra taken in HEPES buffer of TRIS conjugated to 4-MBA with increasing EDC/NHS activation time from 1- 4 hours. The bottom condition tested 1 hour with stirring. Percentage of COO- peak reduction is labeled next to each respective spectrum.

compared to 1hr and a 3.5% increase over 4 hours, therefore giving the highest %COO- peak reduction in only an hour (~50%). These results help indicate that diffusion of the EDC/NHS to the surface was a problem. Taking all this information into account, a 0.1M/0.1M EDC/NHS solution at pH 6.0 (MES buffer) with stirring was used for all future experiments. Despite all the optimization experiments performed, it is important to note that there is still the slight presence of a residual COO- peak present. This may be attributed to the relatively close-packed nature of the substrate used since many of the hot spots generated follow a characteristic long-tail distribution.[36] As a result from a probability stand point, the likelihood of either EDC/NHS or the TRIS molecule (assuming EDC/NHS activated 4-MBA located there) finding these hottest hot spots is relatively low. In addition, these hot-spots are responsible for a significant amount of the generated spectra (47% for EFs >10^8), therefore contributing significantly to the overall background noise.[37] In either

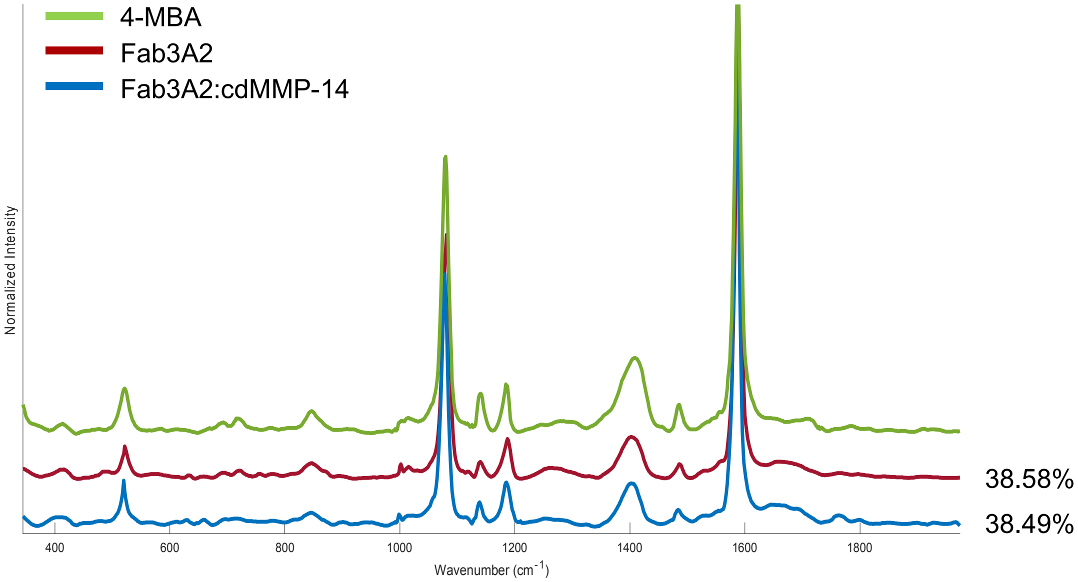

Figure 3-6: SERS spectra of Fab3A2 conjugated to 4-MBA and Fab3A2:cdMMP-14 with percentage of COO- peak reduction labeled next to each respective spectrum.

case, the optimization conditions listed out thus far will provide a good starting platform for highly sensitive SERS sensing of MMP-14.

Fab3A2:cdMMP-14 Sensing:

The conjugation of Fab3A2 along with cdMMP-14 recognition are shown in Figure 3-6, with %COO- peak reduction listed next to each respective spectrum. Both COO- peaks located at 1410cm^{-1}(ν_s(COO-)) and 840cm^{-1}(δ(COO-)) experience the characteristic decrease in peak intensity upon binding with Fab3A2. The peaks located at 1140cm^{-1} (ν_{15}, b$_2$, C-H deformation bending) and 519cm^{-1} (not characterized) also undergo a decrease in intensity with 519cm^{-1} increasing in intensity again as cdMMP-14 is introduced. Although not discussed, these changes in peak intensity match what is observed in previous reported studies.[29-30] A 38.58% reduction was also observed for Fab3A2 binding with a slight

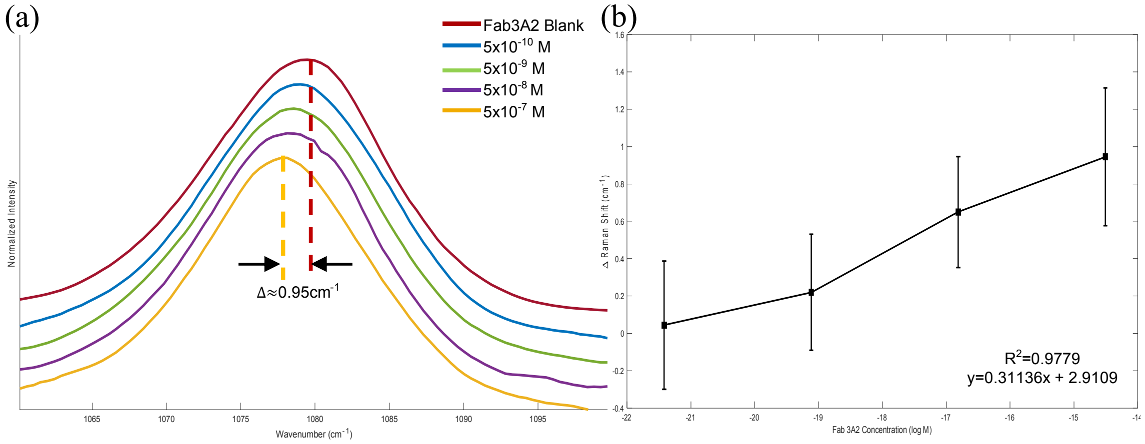

Figure 3-7: (a) SERS spectra of the 4-MBA/Fab3A2 bound substrate after exposure to cdMMP-14 of various concentrations. (b) Semilog plot of the absolute peak shift as a function of cdMMP-14 concentration with respect to the peak located at 1080cm^{-1}.

decrease to 38.49% upon cdMMP-14 recognition, indicating potential non-specific adsorption to the surface. The change in peak frequency with respect to different cdMMP-14 concentrations compared with the Fab3A2 blank sample are shown in Figure 3-7(a). A clear peak shift is observed over the range 10^{-10}M to 10^{-7}M corresponding to a frequency shift of 0.95±0.37cm^{-1} and 0.044±0.34cm^{-1} respectively. The change in peak frequency shift as a function of cdMMP-14 is shown in Figure 3-8(b) showing a linear semilog relationship over this range. The calibration equation $y = 0.31136x + 2.9109$ was obtained, where x represents the logarithmic cdMMP-14 concentration and y is the absolute value of the frequency shift. Using this information, the SERS immunosensor proposed here can be used for the quantitative detection of cdMMP-14 within this concentration range. As concentration increased however, to 10^{-6}M, a slight red shift was observed compared to the peak position at 10^{-7}M. This may be attributed to the fact that Fab3A2 is a suicide inhibitor and can be cleaved by cdMMP-14 at relatively high concentrations and long incubation times.[11] The peak located at 1080cm^{-1} was chosen since it was the most sensitive to

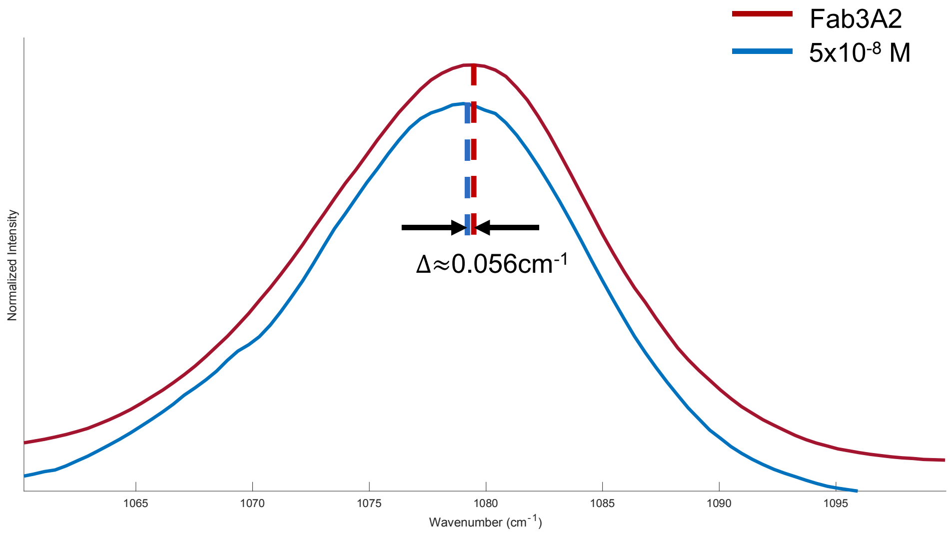

Figure 3-8: SERS spectra of the 4-MBA/Fab3A2 bound substrate after exposure to cdMMP-14.

changes in cdMMP-14 concentration. This peak corresponds to an in-plane ring-breathing mode coupled with the ν(C-S) vibrational mode, making it highly likely that upon binding to Fab3A2, not only is the ring-breathing mode experiencing deformation induced by the high molecular weight of Fab3A2, but so is the benzene thiol sulfur bond (Benzene-S-Ag). As a result, this gives two factors that contribute to the overall frequency shift observed that is missing in the ring breathing mode located at 1589cm^{-1}.

Control Experiments:

To ensure that the observed frequency shift was induced due to Fab3A2:cdMMP-14 recognition and not non-specific adsorption, Fab3A2 was introduced to cdMMP-9 as a negative control experiment with the resulting spectra shown in Figure 3-8. There is a slight down shift of 0.056±0.3cm^{-1} compared to the 0.65±0.3cm^{-1} observed at the same 10^{-8}M concentration for cdMMP-14. Although, Fab3A2 has high specificity towards cdMMP-14, it has been reported to have about a 2.5% binding affinity towards cdMMP-9, which may

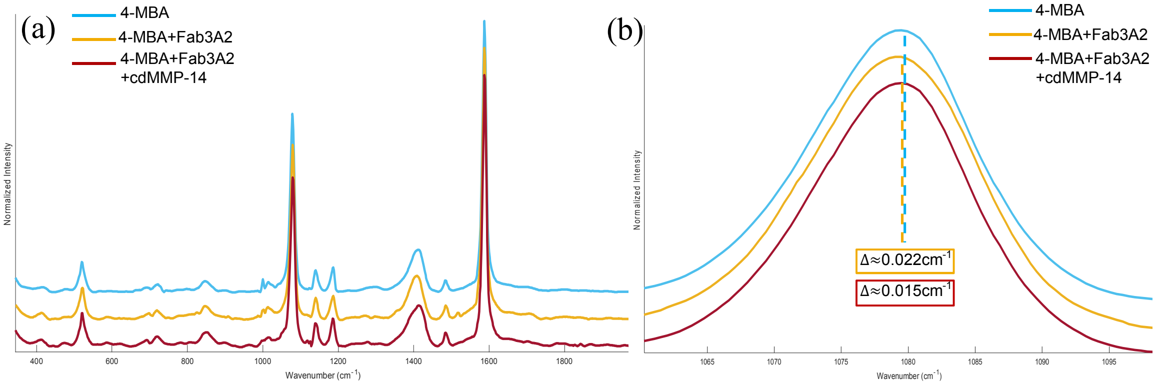

Figure 3-9: (a) SERS spectra of 4-MBA with no EDC/NHS activation after adding Fab3A2 and cdMMP-14. (b) Zoom-in of the spectral region at 1080cm^{-1} with frequency shifts listed after each step.

explain this slight down shift.[23] An additional control experiment was therefore preformed to examine if nonspecific protein adsorption was occurring. An additional control experiment was therefore preformed to examine if nonspecific protein adsorption was occurring. Non-activated 4-MBA LB thin film slides were mixed with Fab3A2, washed, and mixed with 5x10^{-8}M cdMMP-14 as described in the experimental section above. The results shown in Figure 3-9(a) reveal no changes in the spectra after each step, with all intensities roughly consistent with the 4-MBA blank. Looking closer at the 1080cm^{-1} peak shown in Figure 3-9(b) reveals that there is a small shift upwards of about 0.022±0.29cm^{-1} after the addition of Fab3A2, however an even smaller shift of about 0.015±0.3cm^{-1} occurs after rinsing the slide and adding cdMMP-14, then rinsing again. This data helps imply that there is some non-specific adsorption occurring where the last wash step may have removed any residual Fab3A2 and cdMMP-14 that may have been present on the silver surface. Despite this, non-specific adsorption on the LB thin film slide appears to be minimal.

3.4 Conclusions

The sensitive and specific screening of the early stages of metastasis is critical for increasing patient survival rates and for the successful treatment of the disease. In this study, a highly sensitive SERS immunosensor was constructed using 4-MBA functionalized silver octahedral thin film slides conjugated to Fab3A2 and was able to detect the biorecognition of cdMMP-14 via extrinsic nano-stress sensing. Optimization experiments of EDC/NHS using TRIS buffer indicate that for the proposed SERS capture substrate, a 0.1M/0.1M EDC/NHS concentration at pH6.0 with stirring gives the highest percentage of product formation (~50%). Binding of Fab3A2 reveals a maximum of only 38.58% binding with respect to COO- peak reduction. In both cases, this may be the result of the long-tail distribution of highly enhancing hot spots, making the probability of Fab3A2 finding these spots difficult. In addition, these hot spots account for a significant portion of the spectra and are located in the sub-nm gaps between the well-packed octahedral nanoparticles. As a result, it is highly unlikely that Fab3A2 can access these hotspots due to its relatively large size, resulting in the subsequent hydrolysis of any NHS-intermediates, therefore contributing to the background noise and muting the maximum observable peak shift. Despite this, the successful detection of cdMMP-14 was achieved with a maximum frequency shift of 0.95±0.37cm^{-1} for 5x10^{-7}M and a minimum frequency shift of 0.044±0.34cm^{-1} for 5x10^{-10}M. A linear semilog relationship (R^2=97.79%) was observed giving the equation $y = 0.31136x + 2.9109$ within the concentration range. Control experiments shows slight to relatively no binding with cdMMP-9 as well as minimal non-specific protein adsorption.

3.5 References

[1] Siegel, R. L., Miller, K. D., and Jemal, A. "Cancer Statistics 2017". *CA: A Cancer Journal for Clinicians*. 67. 2017. 7-30.

[2] Cronin, K. A., Lake, A. J., Scott, S., Sherman, R.L., Noone, A. M., Howlader, N., Henley, S. J., Anderson, R. N., Firth, A. U., Ma, J., Kohler, B. A., Jemal, A. "Annual Report to the Nation on the Status of Cancer, Part I: National Caner Statistics". *Cancer*. 124. 2018. 2785-2800.

[3] Guan, X. "Cancer Metastases: Challenges and Opportunities". *Acta Pharmaceutica Sinica B*. 5. 2015. 402-418.

[4] Cathcart, J., Pulkoski-Gross, A., and Cao, J. "Targeting Matrix Metalloproteinases in Cancer: Brining New Life to Old Ideas". *Genes & Diseases*. 2. 2015. 26-34.

[5] Nam, D. H., Lee, K. B., and Ge, X. "Functional Production of Catalytic Domains of Human MMPs in Escherichia Coli Periplasm". *Methods in Molecular Biology*. 1731. 2018. 65-72.

[6] Mimori, K., Ueo, H., Shirasaka, C., and Mori, M. "Clinical Significance of MT1-MMP mRNA Expression in Breast Cancer". *Onocology Reports*. 8. 2001. 401-403.

[7] Rundhaug, J. E. "Matrix Metalloproteinases and Angiogenesis". *Journal of Cellular and Molecular Medicine*. 9. 2005. 267-285.

[8] Jiang, A., Lehti, K, Wang, X., Weiss, S. J., Keski-Oja, J., and Pei, D. "Regulation of Membrane-Type Matrix Metalloproteinase 1 Activity by Dynamin-Mediated Endocytosis". *PNAS*. 98. 2001. 13693-13698.

[9] Reunanen, N. and Kahari, V. "Matrix Metalloproteinases in Cancer Cell Invasion". *Madame Curie Bioscience Database*. Austin (TX): Landes Bioscience, 2000-2013. Ebook.

[10] Itoh, Y. "Membrane-Type Matrix Metalloproteinases: Their Functions and Regulations". *Matrix Biology*. 44-46. 2015. 207-223.

[11] Lopez, T. Nam, D. H., Kaihara, E., Mustaga, Z., and Ge, X. "Identification of Highly Selective MMP-14 Inhibitory Fabs by Deep Sequencing". *Biotechnology and Bioengineering*. 114. 2017. 1140-1150.

[12] Tetu, B., Brisson, J., Wang, C. S., Lapointe, H., Beaudry, G. Blanchette, C., and Trudel, D. "The Influence of MMP-14, TIMP-2 and MMP-2 Expression on Breast Cancer Prognosis". *8*. 2005. 1-9.

[13] Adley, B. P., Gleason, K. J., Yang, X. J., and Stack, M. S. “Expression of Membrane Type 1 Matrix Metalloproteinase (MMP-14) In Epithelial Ovarian Cancer: High Level Expression in Clear Cell Carcinoma”. *112*. 2009. 319-324.

[14] Yan, T., Lin, Z., Jiang, J., Lu, S., Chen, M., Que, H., He, X., Que, G., Mao, J., Xiao, J., and Zheng, Q. “MMP14 Regulates Cell Migration and Invasion Through Epithelial-Mesenchymal Transition in Nasopharyngeal Carcinoma”. *American Journal of Translational Research*. 5. 2015. 950-958.

[15] Okudera, K., Kamata, Y., Takanashi, S., Hasegawa, Y., Tsushima, T., Ogura, Y., Nakanishi, K., Sato, H., and Okumura, K. “Small Adenocarcinoma of the Lung: Prognostic Significance of Central Fibrosis Chiefly Because of its Association with Angiogenesis and Lymphangiogenesis,” *Pathology International*. 56. 2006. 494–502.

[16] Nabeshima, K., Inoue, T. Shimao, Y., Okada, Y. Itoh, Y., Seiki, M. Koono, M. “Front-Cell-Specific Expression of Membrane-Type 1 Matrix Metalloproteinase and Gelatinase A During Cohort Migration of Colon Carcinoma Cells Induced by Hepatocyte Growth Factor/Scatter Factor”. *Cancer Research*. 13. 2000. 3364-3369.

[17] Remacle, A. G., Cieplak, P., Nam. D. H., Shiryaev, S. A., Ge, X., and Strongin, A. Y. “Selective Function-Blocking Monoclonal Human Antibody Highlights the Important Role of Membrane Type-1 Matrix Metalloproteinase (MT1-MMP) in Metastasis”. *Oncotarget*. 8. 2017. 2781-2799.

[18] Nam, D. H., Ge, X. “Direct Production of Functional Matrix Metalloproteinase-14 Without Refolding or Activation and Its Application for In Vitro Inhibition Assays”. *Biotechnology and Bioengineering*. 113. 2016. 717-723.

[19] Devy, L. and Dransfield, D. T. “New Strategies for the Next Generation of Matrix-Metalloproteinase Inhibitors: Selectively Targeting Membrane-Anchored MMPs with Therapeutic Antibodies”. *Biochemistry Research International*. 2011. 2010. 1-11.

[20] Decock, J., Thirkettle, S., Wagstaff, L., Edwards, D. R., “Matrix Metalloproteinases: Protective Roles in Cancer”. *Journal of Cellular and Molecular Medicine*. 15. 2011. 1254-65.

[21] McCawley, L. J., Wright, J., LaFleur, B. J., Crawford, H. C., Matrisian, L. M. “Keratinocyte Expression of MMP3 Enhances Differentiation and Prevents Tumor Establishment”. *American Journal of Pathology*. 173. 2008. 1528-39.

[22] Houghton, A. M., Grisolano, J. L., Baumann, M. L., Kobayashi, D. K., Hautamaki, R. D., Nehring, L. C., Cornelius, L. A., Shapiro, S. D. “Macrophage Elastase (Matrix Metalloproteinase-12) Suppresses Frowth of Lung Metastases”. *Cancer Research*. 66. 2006. 6149-55.

[23] Nam, D. H., Rodriguez, C., Remacle, A. G., Strongin, A. Y., and Ge, X. "Active-Site MMP-Selective Antibody Inhibitors Discovered from Convex Paratope Synthetic Libraries". *PNAS*. 113. 2016. 14970-14975.

[24] Lopez-Avila, V. and Spencer, J. V. "Methods for Detection of Matrix Metalloproteinases as Biomarkers in Cardiovascular Disease". *Clinical Medicine: Cardiology*. 2. 2008. 75-85.

[25] Jeon, T. Y., Kim, D. J., Park, S-G., Kim, S-H., and Kim, D-H. "Nanostructured Plasmonic Substrates for Use as SERS Sensors". *Nano Convergence*. 3. 2016. 1-20.

[26] Kho, K.W., Dinish, U.S., Kumar, A., and Olivo, M. "Frequency Shifts in SERS for Biosensing". *ACS Nano*. 6. 2012. 4892-4902.

[27] Perumal, J., Kong, K.V., Dinish, U.S., Bakker, R.M., and Olivo, M. "Design and Fabrication of Random Silver Films as Substrate for SERS Based Nano-Stress Sensing of Proteins". *RCS Advances*. 4. 2014. 12995-13000.

[28] Tang, B., Wang, J., Hutchinson, J. A., Ma, L., Zhang, N., Guo, H., Hu, Z., Li, M., and Zhao, Y. "Ultrasensitive, Multiplex Raman Frequency Shift Immunoassay of Liver Cancer Biomarkers in Physiological Media". *ACS Nano*. 10. 2016. 871-879.

[29] Guerrini, L., Pazos, E., Penas, C., Vazquez, M. E., Mascarenas, J. L., and Alvarez-Pubela, R. A. "Highly Sensitive SERS Quantification of the Oncogenic Protein c-Jun in Cellular Extracts." *JACS*. 135. 2013. 10314-10317.

[30] Ma, H. Sun, X., Chen, L., Cheng, W., Han, X. X., Zhao, B., He, C. "Multiplex Immunochips for High-Accuracy Detection of AFP-L3% Based on Surface-Enhanced Raman Scattering: Implications for Early Liver Cancer Diagnosis". *Analytical Chemistry*. 89. 2017. 8877-8883.

[31] Talley, C. E., Jusinski, L., Hollars, C. W., Lane, S. M., and Huser, T. "Intracellular pH Sensors Based on Surface-Enhanced Raman Scattering". *Analaytical Chemistry*. 76. 2004. 7064-7068.

[32] Ho, C. H., and Lee, S. "SERS and DFT Investigation on the Adsorption Behavior of 4-Mercaptobenzoic Acid on Silver Colloids". *Colloids and Surfaces A: Physiochemical and Engieering Aspects*. 474. 2015. 29-35.

[33] Palazon, F., Benavides, C. M., Leonard, D., Souteytand, E., Checolot, Y., and Colarec, J. P. "Carbodiimide/NHS Derivatization of COOH-Terminated SAMs: Activation or Byproduct Formation?". *Langmuir*. 30. 2014. 4545-4550.

[34] Wang, C., Yan, Q., Liu, H. B., Zhou, X. H., and Xiao, S. J. “Different EDC/NHS Activation Mechanisms between PAA and PMAA Brushes and the Following Amidation Reactions”. *Langmuir*. 27. 2011. 12058-12068.

[35] Sam, S., Touahir, L., Andresa, J. S., Allongue, P., Chazalviel, J. N., Gouget-Laemmel, A. C., Henry de Villeneuve, C., Moraillon, A., Ozanam, F., Gabouze, N., and Djebbar, S. “Semiquantitative Study on the EDC/NHS Activation of Acid Terminal Groups at Modified Porous Silicon Surfaces”. *Langmuir.* 26. 2010. 809-814.

[36] Le Ru, E. C., Etchegoin, P. G., and Meyer, M. “Enhancement Factor Distribution Around a Single Surface-Enhanced Raman Scattering Hot Spot and its Relation to Single Molecule Detection”. *The Journal of Chemical Physics*. 125. (2006). 204701.

[37] Fang, Y., Seong, N. H., and Dlott, D. D. “Measurement of the Distribution of Site Enhancements in Surface-Enhanced Raman Scattering”. *Science*. 321. 2008. 388-391.

Chapter 4: Conclusions and Future Work

Biosensors are finding increasing impact in a variety of fields ranging from material science to biomedical as a popular method to achieve rapid, high-throughput, ultrasensitive sensing. This application has attracted significant attention from the medical field as a possible means for early cancer screening and diagnosis. Current cancer screening methods and imaging are in need of significant improvement as most require tissue biopsy's, significantly high concentrations of cancer cells or related biomarkers, or are only observable when visible changes to the tissue have already occurred.[1-2] In fact, the current threshold for clinical imaging requires for 1cm^3 of localized tumor cells (10^9 cells) in order to reliably diagnose the cancer[1], with the death rate increasing about 1.3% per millimeter increase.[3] In addition, they are often riddled with high false-positive rates[4-5], which can lead to highly invasive procedures and follow-ups, causing unneeded stress on the patient. As a result, there is an urgent need for a reliable, ultrasensitive sensing platform that can go beyond the current limitations of liquid biopsies. Since 90% of all cancer related deaths are due to metastasis, targeting and inhibiting its early stages should help correlate with increased patient survivability and resulting disease prognosis.[3] MMP-14 has become a popular target of interest due to its ability to induce tissue remodeling, extracellular matrix degradation, tumor invasion and angiogenesis.[6-7] The development of Fab3A2 has allowed for the highly selective inhibition of MMP-14 and can also be used to detect elevated levels in patients as an early cancer screening method. Coupling this with the signal amplification offered by SERS and the sensitivity from a novel nano-stress mechanism can allow for the development of a highly sensitive SERS immunosensor.

In chapter 2, well-defined, high quality Ag octahedral nanocrystals were synthesized in large quantities using a modified polyol process and were reliably assembled into large-scale, close-packed, two-dimensional LB thin films using a homemade LB trough. The presence of many polycrystalline well-ordered, close-packed domains were observed, which can contribute significantly to the overall optical signal enhancement. In addition, the whole process was completed using cost-effective equipment and laboratory procedures.

In chapter 3, EDC/NHS optimization tests indicate that a 0.1M/0.1M EDC/NHS solution at pH 6.0 with stirring gives the highest conjugation to the 4-MBA surface using TRIS (~50%). Using these conditions, 38.58% of Fab3A2 was successfully conjugated to the 4-MBA surface and was characterized by comparing peak intensity of the COO- peak located at 1410cm^{-1} before and after attachment. By observing peak shift at 1080cm^{-1} the binding recognition of cdMMP-14 was observed with a maximum and minimum frequency shift of 0.95±0.37cm^{-1} and 0.044±0.34cm^{-1} for cdMMP-14 at concentrations 5x10^{-7}M and 5x10^{-10}M respectively. A linear semilog relationship (R^2=97.79%) was observed giving the equation $y = 0.31136x + 2.9109$ within the concentration range. Control experiments shows slight to relatively no binding with cdMMP-9 as well as minimal non-specific protein adsorption thereby completing the proof-of-concept SERS immunosensor platform.

Although a peak shift was observed, it is relatively small, as is the observed percentage of Fab3A2 bound to the surface (38.58% vs. 49.44% from TRIS). As mentioned prior, the "hottest" hotspots that offer the highest signal enhancement and therefore a significant contribution to the SERS spectrum, are located between the sub-nm gaps generated from the close-packed film. This makes it highly unlikely for relatively large molecule such as Fab3A2 to be able to access these hotspots therefore leaving them unreacted where they can hydrolyze back into unwanted carboxyl groups. These hotspots also follow a long-tail distribution, making it very difficult for them to be activated statistically in the first place. As a result, optimizing the octahedral silver nanoparticle distance should help resolve this issue. By increasing the interparticle distance slightly, we can allow more room for the Fab3A2 molecule (and other antibodies) to access while still retaining a relatively high enhancement factor. Utilizing the LB process should allow for easy manipulation of particle spacing and subsequent plasmonic tunability. Hopefully the work accomplished herein may serve as platform for my group and other researchers towards developing early cancer screening methods and that eventually, the proposed highly sensitive immunosensor may find use in clinical settings towards the early detection of metastasis.

4.1 References:

[1] Frangioni, J.V. “New Technologies for Human Cancer Imaging”. *Journal of Clinical Oncology*. 26. 2008. 4012-4021.

[2] Kalinich, M. and Haber, D.A. “Cancer Detection: Seeking Signals in Blood”. *Science*. 359. 2018. 866-867.

[3] Guan, X. “Cancer Metastases: Challenges and Opportunities”. *Acta Pharmaceutica Sinica B*. 5. 2015. 402-418.

[4] Croswell, J. M., Baker, S. G., Marcus, P. M., Clapp, J. D., Kramer, B. S. “Cumulative Incidence of False-Positive Test Results in Lung Cancer Screening: A Randomized Trial”. *Ann Intern Med*. 152. 2010. 505-512.

[5] Wang, L. “Early Diagnosis of Breast Cancer”. *Sensors*. 17. 2017. 1572-1592.

[6] Reunanen, N. and Kahari, V. “Matrix Metalloproteinases in Cancer Cell Invasion”. *Madame Curie Bioscience Database*. Austin (TX): Landes Bioscience, 2000-2013. Ebook.

[7] Itoh, Y. “Membrane-Type Matrix Metalloproteinases: Their Functions and Regulations”. *Matrix Biology*. 44-46. 2015. 207-223.